

# Velocity perturbations and Reynolds stresses in Holmboe instabilities

Cite as: Phys. Fluids **34**, 074110 (2022); doi: [10.1063/5.0097624](https://doi.org/10.1063/5.0097624)

Submitted: 30 April 2022 · Accepted: 11 June 2022 ·

Published Online: 8 July 2022



View Online



Export Citation



CrossMark

Adam J. K. Yang (杨健康),<sup>1,a)</sup>  E. W. Tedford,<sup>1</sup> J. Olsthoorn,<sup>1,2</sup>  A. Lefauve,<sup>3</sup>  and G. A. Lawrence<sup>1</sup> 

## AFFILIATIONS

<sup>1</sup>Department of Civil Engineering, University of British Columbia, Vancouver, British Columbia V6T1Z4, Canada

<sup>2</sup>Department of Civil Engineering, Queen's University, Kingston, Ontario K7L 3N6, Canada

<sup>3</sup>Department of Applied Mathematics and Theoretical Physics, University of Cambridge, Cambridge CB3 0WA, United Kingdom

<sup>a)</sup>Author to whom correspondence should be addressed: [jyangay@mail.ubc.ca](mailto:jyangay@mail.ubc.ca)

## ABSTRACT

The velocity perturbations and Reynolds stresses associated with finite-amplitude Holmboe instabilities are investigated using linear stability analysis, numerical simulations, and laboratory experiments. The rightward and leftward propagating Holmboe instabilities are separated, allowing for a direct comparison of the perturbation fields between the numerical simulations and the linear stability analysis. The decomposition and superposition of the perturbation fields provide insights into the structure and origin of Reynolds stresses in Holmboe instabilities. Shear instabilities in stratified flows introduce a directional preference (anisotropy) in velocity perturbation fields, thereby generating Reynolds stresses. Here, we investigate this anisotropy by comparing pairs of horizontal and vertical velocity perturbations ( $u'$ ,  $w'$ ), obtained from the simulations and the laboratory experiment, with predictions from linear stability analysis. For an individual Holmboe mode, both the simulations and linear theory yield elliptical ( $u'$ ,  $w'$ )-pairs that are oriented toward the second and fourth quadrants ( $u'w' < 0$ ), corresponding to the tilted elliptical trajectories of particle movement. Combining the leftward and rightward Holmboe modes yields ( $u'$ ,  $w'$ ) ellipses whose orientation and aspect ratio are phase-dependent. When averaged over a full cycle, the joint probability density functions of ( $u'$ ,  $w'$ ) in the linear theory and single wavelength simulations exhibit “steering wheel” structures. This steering wheel is smeared out in multiple wavelength simulations and the laboratory experiment due to varying wavelengths, resulting in an elliptical cloud. All of the approaches adopted in the present study yield Reynolds stresses that are comparable to those reported in previous laboratory and field investigations.

Published under an exclusive license by AIP Publishing. <https://doi.org/10.1063/5.0097624>

## I. INTRODUCTION

The onset of instabilities triggering non-linear motions is a fundamental problem in fluid mechanics. In density-stratified shear flows, the Kelvin–Helmholtz instability and the lesser-known Holmboe instability can occur. The Kelvin–Helmholtz instability occurs when the thickness of the density interface is similar to that of the velocity interface and is characterized by periodic arrays of billows.<sup>1,2</sup> The Holmboe instability occurs when the density interface is much thinner than the velocity interface and is characterized by two counter-propagating waves that develop on either side of the density interface.<sup>3–6</sup> The Holmboe instability occurs in the ocean surface mixed layer<sup>7</sup> and near deep-ocean topography,<sup>8</sup> in atmospheric jets and fronts,<sup>9</sup> in estuarine salt wedges,<sup>10–12</sup> in river outflows,<sup>13</sup> and in pyroclastic currents.<sup>14</sup> While the Kelvin–Helmholtz instability has traditionally been studied more extensively,<sup>15</sup> in recent years, increasing attention has been paid to the Holmboe instability. An improved understanding of the Holmboe instability has a wide range of

applicability from the prediction of salt water intrusion into estuaries<sup>16</sup> to the sub-grid scale parameterization of mass, momentum, and energy transfers in general circulation models.<sup>17,18</sup>

Our understanding of the Holmboe instability has been advanced by comparing the results of two-dimensional linear stability analysis with numerical simulations, laboratory experiments, and field studies. There has been good agreement between the predicted linear growth rates of Holmboe instabilities and the results of numerical simulations.<sup>15,19</sup> There has also been good agreement between the predictions of linear stability analysis and observations of phase speeds and wavelengths of finite-amplitude Holmboe instabilities in laboratory experiments.<sup>20–25</sup> In addition, the vertical location and wavelength of finite-amplitude Holmboe instabilities observed in the Fraser River salt wedge coincide with the predictions of linear stability analysis.<sup>10,26,27</sup> The relevance of linear stability analysis to finite-amplitude Holmboe instabilities is thought to be a consequence of the general observation that infinitesimal perturbations pass through a

sequence of bifurcations to reach finite-amplitude coherent states and, in the process, retain some of their key properties.<sup>28</sup> The above observations have motivated us to investigate the extent to which linear stability analysis can provide insight into the properties of the velocity perturbations and Reynolds stresses associated with finite-amplitude Holmboe instabilities.

In stratified shear flows in general, stratification and horizontal shear inevitably introduce a directional preference (anisotropy) in the velocity perturbation fields, thereby generating Reynolds stresses.<sup>29–33</sup> Scatter plots of the horizontal and vertical velocity perturbation pairs ( $u'$ ,  $w'$ ) have been used to show the degree of anisotropy and estimate the Reynolds stresses, which describe momentum and kinetic energy transfer.<sup>34–36</sup> These scatter plots yield anisotropic clouds of points often fitted with variance ellipses.<sup>35,37</sup> These variance ellipses are characterized by the orientation angle and anisotropy and determine the Reynolds stresses. Although the link between variance ellipses and fluid motions is unclear, the variance ellipse has been extensively used to investigate barotropic and baroclinic instabilities due to its geometric simplicity.<sup>37–41</sup>

In the present paper, we compare the variance ellipses and Reynolds stresses of Holmboe instabilities obtained using linear stability analysis with those obtained from numerical simulations and laboratory experimentation. To do so, we focus on the flow field of two-dimensional coherent structures associated with the Holmboe instability at moderate Reynolds numbers ( $10^2$ – $10^3$ ). We will address (i) how the variance ellipses and the resulting Reynolds stresses vary vertically, (ii) how these relate to the fluid motion, and (iii) how they vary in progressively more realistic systems, i.e., from idealized linear stability analysis to single wavelength simulations, multiple wavelength simulations, and laboratory experiments. Unlike the commonly used single wavelength simulations with a constant wavelength, the multiple wavelength simulations allow for the spatial and temporal variation of wavelengths as is observed in laboratory experiments<sup>20,22–25</sup> and field observations.<sup>10–12,42</sup>

Section II describes the background for our linear stability analysis and numerical simulations. In Sec. III, we present the horizontal and vertical velocity perturbation pairs associated with each of the counter-propagating wave modes predicted by linear stability analysis and the resultant Reynolds stresses. We then present the phase-dependent interaction between the counter-propagating waves. Section IV presents the Reynolds stresses computed using numerical simulations. By comparing single and multiple wavelength simulations, we examine wavenumber shifting and its effects on the instabilities from linear growth to saturation. In Sec. V, we compare the velocity perturbation pairs and Reynolds stresses predicted by linear stability theory with numerical simulations and a laboratory experiment. Our summary and conclusions are presented in Sec. VI.

## II. BACKGROUND

### A. Setup and equations

A density-stratified shear layer consists of initial velocity and density profiles whose variation in the vertical direction can be represented by hyperbolic tangent functions. The velocity distribution has a total jump  $\Delta U$  over a length scale  $h$ . Similarly, the stable density distribution has a total jump  $\Delta \rho$  over a length scale  $\delta$ ,

$$\bar{U}(z) = \frac{\Delta U}{2} \tanh\left(\frac{2}{h}z\right), \quad (1)$$

$$\bar{\rho}(z) = -\frac{\Delta \rho}{2} \tanh\left(\frac{2}{\delta}z\right). \quad (2)$$

A schematic illustrating these profiles is shown in Fig. 1(a). The shear layer (vorticity) thickness is  $h \equiv \Delta U / (d\bar{U}/dz)_{\max}$ , and the density layer thickness is  $\delta \equiv \Delta \rho / (d\bar{\rho}/dz)_{\max}$ . These idealized hyperbolic tangent profiles have been used extensively in the literature,<sup>43–47</sup> since they closely approximate the background profiles in many stratified flows in nature. Based on these scales, we define four dimensionless parameters: the Reynolds number ( $Re$ ), the bulk Richardson number ( $J$ ), the Schmidt number ( $Sc$ ), and the thickness ratio ( $R$ ) as

$$Re \equiv \frac{\Delta U h}{\nu}, \quad (3)$$

$$J \equiv \frac{\Delta \rho g h}{\rho_0 (\Delta U)^2}, \quad (4)$$

$$Sc \equiv \frac{\nu}{D}, \quad (5)$$

$$R \equiv \frac{h}{\delta}, \quad (6)$$

where  $\nu$  is the kinematic viscosity and  $D$  is the diffusivity.

The dimensionless Navier–Stokes equations under the Boussinesq approximation are

$$\nabla \cdot \mathbf{u} = 0, \quad (7)$$

$$\frac{\partial \mathbf{u}}{\partial t} + \mathbf{u} \cdot \nabla \mathbf{u} = -\nabla p - J \rho \mathbf{k} + Re^{-1} \nabla^2 \mathbf{u}, \quad (8)$$

$$\frac{\partial \rho}{\partial t} + \mathbf{u} \cdot \nabla \rho = (Re Sc)^{-1} \nabla^2 \rho, \quad (9)$$

where  $\mathbf{u}$  is the velocity vector,  $p$  is the pressure,  $\rho$  is the density, and  $\mathbf{k}$  is the unit vertical vector.

### B. Linear stability analysis

We solve the linearized Navier–Stokes equations (7)–(9) based on the assumptions of a parallel background mean flow and two-dimensional perturbations with normal mode forms (e.g., Refs. 19 and 48–50). The full velocity, pressure, and density fields are expressed in terms of the background field and a small superimposed perturbation (i.e.,  $|u'|/\bar{U}| \ll 1$ ),

$$\begin{aligned} \mathbf{u} &= \bar{U}(z) \mathbf{i} + \mathbf{u}'(x, z, t), \\ p &= \bar{P}(z) + p'(x, z, t), \\ \rho &= \bar{\rho}(z) + \rho'(x, z, t), \end{aligned} \quad (10)$$

with all perturbations having the normal mode form

$$\psi'(x, z, t) \equiv \Re\{\hat{\psi}(z) \exp(ikx + \sigma t)\}, \quad (11)$$

where  $\Re$  is taking the real part;  $\hat{\psi}$ ,  $\sigma \in \mathbb{C}$  and  $k \in \mathbb{R}$  is the wavenumber; and  $\mathbf{i}$  is the unit horizontal vector. Note that in numerical simulations,  $\bar{U}$  varies slowly in time due to diffusion of the background profiles.<sup>51</sup> Substituting into the governing Eqs. (7)–(9) yields

$$\sigma \begin{bmatrix} \nabla^2 & \\ & 1 \end{bmatrix} \begin{bmatrix} \hat{w} \\ \hat{\rho} \end{bmatrix} = \begin{bmatrix} \mathcal{L}_w & \mathcal{L}_{w\rho} \\ \mathcal{L}_{\rho w} & \mathcal{L}_\rho \end{bmatrix} \begin{bmatrix} \hat{w} \\ \hat{\rho} \end{bmatrix}, \quad (12)$$

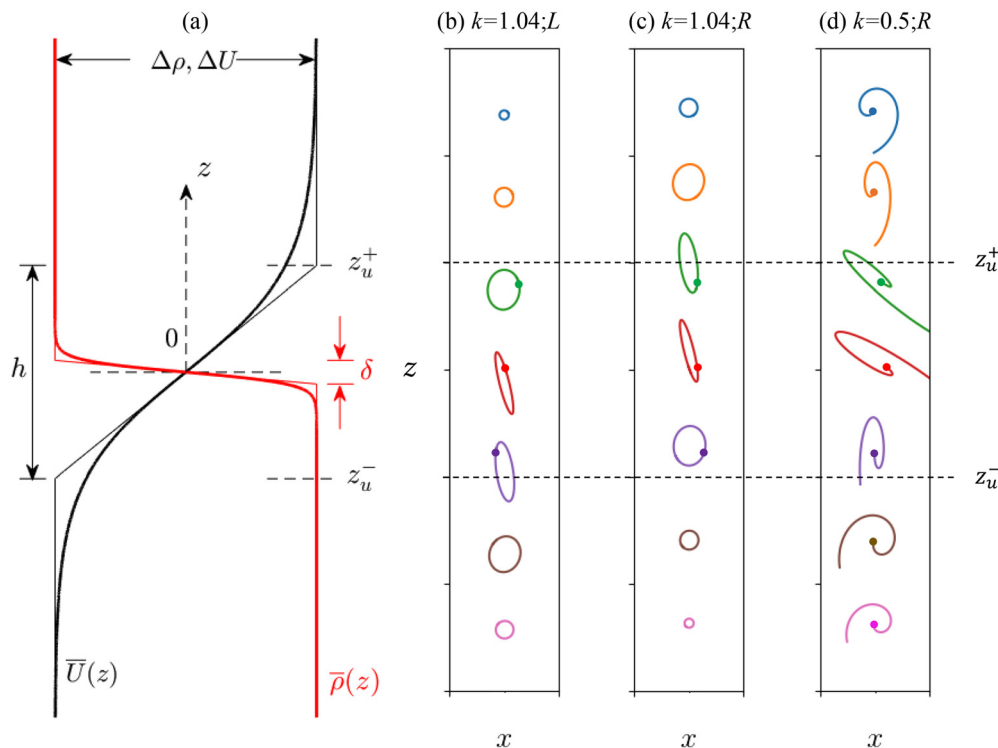


**FIG. 1.** (a) Schematic illustrating the velocity and density profiles. The thick lines are smooth hyperbolic tangent profiles, and the thin lines are the corresponding piecewise linear profiles. The density and velocity profiles are centered at  $z = 0$ . (b)–(d) Fluid particle orbits generated by Holmboe waves in linear stability analysis based on the background profiles in (a). The Holmboe wave is unstable for  $0.01 < k < 1.04$  (most unstable for  $k = 0.5$ ). At  $k = 1.04$ , either circular or elliptical particle orbits are generated for (b) leftward and (c) rightward propagating marginally stable waves. (d) The spiral particle orbits for the rightward propagating unstable wave at  $k = 0.5$ . The dots denote the initial locations. The centroid of particle orbits at all levels is set at  $x = 0$  for comparative purposes.  $L$  and  $R$  represent the leftward and rightward propagating waves, respectively. Note that the particle orbits for the leftward propagating waves (b) mirror those of the rightward propagating waves (c).

where

$$\begin{aligned}\mathcal{L}_w &= -ik\bar{U}\nabla^2 + ik\frac{\partial^2 \bar{U}}{\partial z^2} + Re^{-1}\nabla^4, \\ \mathcal{L}_\rho &= -ik\bar{U} + (ReSc)^{-1}\nabla^2, \\ \mathcal{L}_{w\rho} &= J\left(\frac{\partial^2}{\partial z^2} - \nabla^2\right), \\ \mathcal{L}_{\rho w} &= -\frac{\partial \bar{\rho}}{\partial z},\end{aligned}\tag{13}$$

and  $\nabla^2 = -k^2 + \partial^2/\partial z^2$ ,  $\nabla^4 = k^4 + \partial^4/\partial z^4 - 2k^2 + \partial^2/\partial z^2$ . The streamwise velocity eigenfunction is then reduced to  $\hat{u} = (i/k)\partial\hat{w}/\partial z$ . The eigenvalue can be decomposed as  $\sigma = \sigma_r + i\sigma_i$ , where  $\sigma_r \in \mathbb{R}$  represents the growth rate of the instability and  $\sigma_i \in \mathbb{R}$  is related to the phase speed  $c_p = -\sigma_i/k$ . At the upper and lower boundaries, a no-flux boundary condition is imposed. Free-slip boundary conditions are imposed for comparison with the numerical simulations, and no-slip boundary conditions are imposed for comparison with the laboratory experiment.

### III. LINEAR STABILITY PREDICTIONS

In this section, we use linear stability theory to examine the particle orbits and Reynolds stresses associated with counter-propagating Holmboe waves. We highlight that the total Reynolds stress is equal to

the sum of phase-independent contributions by the rightward and leftward propagating waves, and a phase-dependent interaction between them.

### A. Particle orbits of Holmboe waves

Following the normal mode assumption, the velocity perturbations for a given mode are expressed as

$$u'(x, z, t) \equiv \frac{1}{2} \left[ \hat{u}(z) e^{i(kx - \omega t)} + c.c. \right], \quad (14a)$$

$$w'(x, z, t) \equiv \frac{1}{2} \left[ \hat{w}(z) e^{i(kx - \omega t)} + c.c. \right], \quad (14b)$$

where  $\omega$  ( $= i\sigma$ ) is the frequency and *c.c.* denotes the complex conjugate.

The corresponding linearized movement of fluid particles is then given by<sup>36</sup>

$$\frac{dx_p(t)}{dt} = u'(x_0, z_0, t), \quad (15a)$$

$$\frac{dz_p(t)}{dt} = w'(x_0, z_0, t), \quad (15b)$$

where  $\mathbf{x}(t) = x_p(t)\mathbf{i} + z_p(t)\mathbf{k}$  and  $(x_0, z_0)$  is the initial location.

Figures 1(b) and 1(c) show the orbits of fluid particles (pathlines) for the stable and unstable Holmboe waves. These orbits are obtained from the time integration of Eq. (15) at different initial vertical levels,  $z_0$ . The background profile for the linear stability analysis is the same as that used in the numerical simulations (see Table I). As in the classical stability diagram (e.g., in Ref. 43, see Fig. 13), a positive growth rate for the unstable Holmboe wave exists for  $0.01 < k < 1.04$ , with  $k = 0.5$  being the most unstable wavenumber and  $k = 0.01$  and  $k = 1.04$  are the wavenumbers of marginal instability.

The marginally stable waves exhibit closed particle orbits, whereas the unstable waves exhibit open particle orbits due to the positive growth rate. The particle orbits of both stable and unstable waves are often tilted toward the second and fourth quadrants (Fig. 1), as are the corresponding  $(u', w')$ -pairs. The degree of tilt depends upon the vertical location. For leftward propagating waves, the tilt is prominent within the shear layer below the density interface,  $z_u \lesssim z \lesssim 0$  [Fig. 1(b)], whereas for rightward propagating waves, the tilt is prominent within the shear layer above the density interface,  $0 \lesssim z \lesssim z_u^+$  [Figs. 1(c) and 1(d)]. This tilting generates Reynolds stresses  $\overline{u'w'}$  and will be investigated using both linear stability analysis and numerical simulations.

## B. Interaction of counter-propagating Holmboe waves

To determine Reynolds stresses, using linear stability theory, we examine the interaction of the leftward and rightward propagating Holmboe modes,

$$u' = u'^{(L)} + u'^{(R)}, \quad w' = w'^{(L)} + w'^{(R)}, \quad (16)$$

where the superscripts (L) and (R) are the components corresponding to the leftward and rightward propagating modes, respectively.

The total velocity perturbations can be rewritten as

$$u' = \frac{1}{2} \left[ \hat{u}^{(L)}(z) e^{i(k_L x - \omega_L t)} + c.c. \right] + \frac{1}{2} \left[ \hat{u}^{(R)}(z) e^{i(k_R x - \omega_R t)} + c.c. \right], \quad (17)$$

and  $w'$  has the same form;  $k_L$  ( $k_R$ ) and  $\omega_L$  ( $\omega_R$ ) are the wave number and frequency for the leftward (rightward) propagating waves.

To focus on the interaction between the two waves independent of their growth, we set growth rates to zero ( $\omega_L, \omega_R \in \mathbb{R}$ ). This is consistent with statistical stationarity as commonly assumed in studies of stratified shear flow (e.g., Refs. 29 and 52–54).

Then, we have  $k_L = k_R = k$  and  $\omega_L = -\omega_R = \omega$  for the symmetric Holmboe waves. The total horizontally averaged Reynolds stress over one wavelength is then expressed as

**TABLE I.** The parameters for the numerical simulations. The number of grid points in each direction is  $N_x$ ,  $N_y$ , and  $N_z$ . The initial  $Re_0 = 120$ ,  $J_0 = 0.13$ ,  $Sc = 256$ , and  $R_0 = 9$  were used.  $k_{initial}$  is the initial wavenumber of the maximum growth and  $\lambda_0 = 2\pi/k_{initial}$ . As the background flow evolves over time, the nondimensional numbers ( $Re$ ,  $J$ , and  $R$ ) and the wavenumber of the maximum growth ( $k_{max}$ ) vary accordingly. SWS (MWS) denotes a single wavelength simulation (multiple wavelength simulation).

Run	Initial parameters				Quasi-steady period			
	$Re_0$	$N_x \times N_y \times N_z$	$k_{initial}$	$L_x/\lambda_0$	$t$	$Re$	Observed $k^a$	Figure
SWS (2D)	120	$128 \times 1 \times 512$	0.5	1	120–200	440–560	0.5	2–4, 6–8
SWS (3D)	120	$128 \times 128 \times 512$	0.5	1	120–200	440–560	0.5	8
MWS (2D)	120	$2048 \times 1 \times 512$	0.5	16	250–330	600–740	0.31	5, 6, 8

<sup>a</sup>This wavenumber is calculated based on the observed number of waves in the domain.

$$\begin{aligned} \langle u'w' \rangle_x = & \frac{1}{4} [\hat{u}^{(L)} \hat{w}^{*(L)} + \hat{u}^{*(L)} \hat{w}^{(L)} + \hat{u}^{(R)} \hat{w}^{*(R)} + \hat{u}^{*(R)} \hat{w}^{(R)}] \\ & + \frac{1}{4} \mathcal{R} \left\{ \underbrace{(\hat{u}^{*(L)} \hat{w}^{(R)} + \hat{u}^{(R)} \hat{w}^{*(L)}) e^{2i\omega t}}_{\text{Phase Dependent 1}} \right. \\ & \left. + \underbrace{(\hat{u}^{(L)} \hat{w}^{*(R)} + \hat{u}^{*(R)} \hat{w}^{(L)}) e^{-2i\omega t}}_{\text{Phase Dependent 2}} \right\}. \end{aligned} \quad (18)$$

One may write  $\hat{u} = \hat{u}_r + i\hat{u}_i$  and  $\hat{w} = \hat{w}_r + i\hat{w}_i$  ( $\hat{u}_r, \hat{u}_i, \hat{w}_r, \hat{w}_i \in \mathbb{R}$ ), then the “Phase Dependent 1” and “Phase Dependent 2” terms are a pair of complex conjugates, and thus, we have

$$\begin{aligned} \langle u'w' \rangle_x = & \frac{1}{4} \hat{u}^{(L)} \hat{w}^{*(L)} + \hat{u}^{*(L)} \hat{w}^{(L)} + \frac{1}{4} \hat{u}^{(R)} \hat{w}^{*(R)} + \hat{u}^{*(R)} \hat{w}^{(R)} \\ \text{Total} & \quad \quad \quad \text{Left, } \langle u'w' \rangle_{x:L} \quad \quad \quad \text{Right, } \langle u'w' \rangle_{x:R} \\ & + \frac{1}{2} \mathcal{R} \left\{ \underbrace{(\hat{u}^{*(L)} \hat{w}^{(R)} + \hat{u}^{(R)} \hat{w}^{*(L)}) e^{i\phi}}_{\text{Phase Dependent}} \right\}, \end{aligned} \quad (19)$$

where  $\hat{u}^*$  ( $\hat{w}^*$ ) is the complex conjugate of  $\hat{u}$  ( $\hat{w}$ ) and  $\langle \cdot \rangle_i$  represents an average in the direction  $i$ ; the time dependent variable is  $\phi = 2\omega t$ .

Here, the first line on the right-hand side of Eq. (19) is identical to the horizontally averaged Reynolds stress for the leftward propagating and rightward propagating modes, while the second line is an additional phase-dependent term generated from the superposition of the leftward and rightward propagating waves.

For an individual mode, the Reynolds stress does not have a phase-dependent term. Averaging in the  $x$  and/or  $t$  over a wave cycle for the leftward propagating wave yields

$$\langle u'w' \rangle_{x:L} = \langle u'w' \rangle_{t:L} = \langle u'w' \rangle_{xt:L} = \frac{1}{4} (\hat{u}^{(L)} \hat{w}^{*(L)} + \hat{u}^{*(L)} \hat{w}^{(L)}), \quad (20)$$

and the averaged Reynolds stress for the rightward propagating wave has the same form. All products depend on  $z$  only, and are independent of  $x$  and  $t$ .

Further taking an average of Eq. (19) over one wave period gives us

$$\langle u'w' \rangle_{xt} = \langle u'w' \rangle_{xt:L} + \langle u'w' \rangle_{xt:R}. \quad (21)$$

Figures 2(a)–2(d) show the evolution of different terms in Eq. (19) of the Reynolds stress throughout a cycle given by linear stability analysis. In panel (a), although the perturbations spend an equal amount of time in the growth and decay portions of the cycle, the amplitude of  $\langle u'w' \rangle_x$  is largest when it is negative. Thus, a net negative

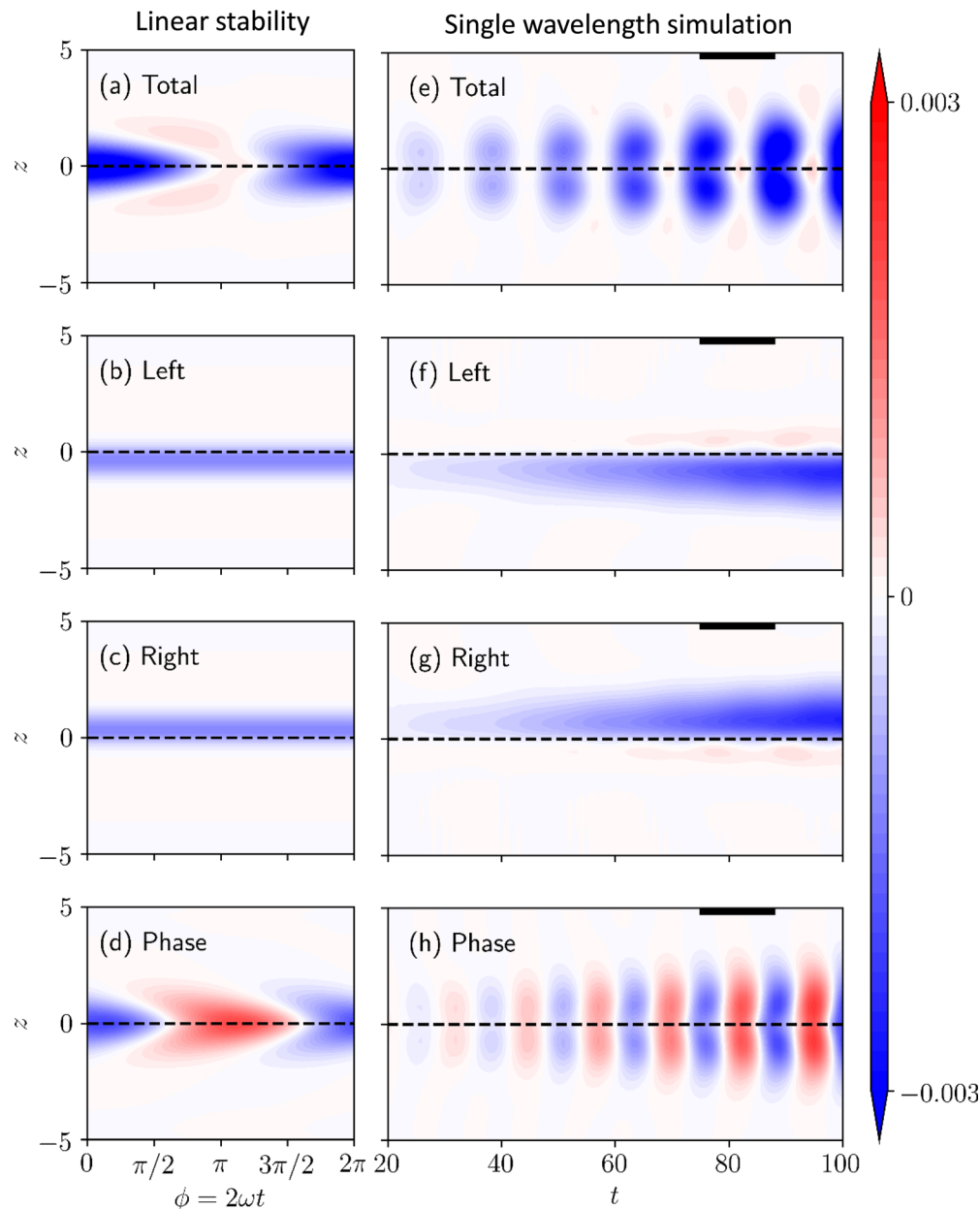


**FIG. 2.** Reynolds stress ( $\langle u'w' \rangle_x$ ) terms in Eq. (19) within one wave period from linear stability analysis (the left column) and  $\langle u'w' \rangle_x$  terms in the non-linear single wavelength simulation (the right column). (a) and (e) The total field, (b) and (f) the leftward propagating wave field, (c) and (g) the rightward propagating wave field, and (d) and (h) the "Phase Dependent" term. The background profile for the linear stability analysis is the same as the initial profile in the single wavelength simulation in Table I. In the simulation, the period under the black solid line was compared with linear stability analysis in Fig. 4.

total Reynolds stress  $\langle u'w' \rangle_{xt}$  is produced. As demonstrated theoretically, this Reynolds stress  $\langle u'w' \rangle_{xt}$  is a sum of time-independent  $\langle u'w' \rangle_{x;L}$  and  $\langle u'w' \rangle_{x;R}$  as shown in panels (b) and (c), respectively. The Reynolds stresses for the rightward and leftward propagating waves are concentrated above and below the density interface, respectively, and they are independent of time.

The additional phase-dependent term is shown in Fig. 2(d). Its cycle illustrates that the magnitude is equally distributed between a

decay period ( $0 \leq \phi < \pi$ ) and a growth period ( $\pi \leq \phi < 2\pi$ ). Over one period, its net contribution to the Reynolds stress is zero. It should be noted that the maximum value of the phase-dependent term is larger than the magnitude of the time averaged  $\langle u'w' \rangle_{xt}$ , which results in  $\langle u'w' \rangle_x$  being positive at some instants (e.g.,  $\phi = \pi$ ). These oscillating patterns are also observed in numerical simulations. We will compare the linear stability analysis with the numerical simulation results in Sec. IV A 2.



#### IV. NUMERICAL SIMULATIONS

We perform numerical simulations using SPINS, a parallelized pseudospectral solver (see Subich *et al.*<sup>55</sup>) to solve the Navier–Stokes equations (7)–(9). The computational domain height is  $L_z = 20$ , which prevents the boundaries from interfering with the shear layer during the linear development.<sup>49</sup> The horizontal length of the domain is  $L_x = \lambda_0$  (the wavelength of the maximum growth rate) in single wavelength simulations and is  $L_x = 16\lambda_0$  in the multiple wavelength simulation. The width in the spanwise direction is  $L_y = 10$  for the three-dimensional simulation.

Periodic boundary conditions were imposed in the horizontal and spanwise directions, and free slip and no flux boundary conditions are imposed at  $z = \pm 10$ . A third-order Runge–Kutta time-stepping scheme was used.  $N_x$ ,  $N_y$ , and  $N_z$  are the number of grid points in the horizontal, spanwise, and vertical directions, respectively. For the two-dimensional single wavelength simulation, multiple wavelength simulation, and the three-dimensional single wavelength simulation, the grids are  $(N_x \times N_z) = (128 \times 512)$ ,  $(N_x \times N_z) = (2048 \times 512)$ , and  $(N_x \times N_y \times N_z) = (128 \times 128 \times 512)$ , respectively. Doubling the number of points in each direction produced results with less than 0.1% difference in the kinetic energy of the instability. The initial  $J_0 = 0.13$  and  $R_0 = 9$ . In this configuration, Holmboe waves appear as the dominant shear instability.<sup>56</sup> The initial  $Re_0 = 120$  increases several-fold as the background profiles diffuse vertically (see Table I).

To provide an optimal comparison with the linear stability theory, the two-dimensional and three-dimensional single wavelength simulations were run with an eigenfunction perturbation,<sup>51</sup> which was associated with the wavenumber of maximum growth rate. The perturbation, with the superposition of the leftward and rightward modes, was obtained through linear stability described above, having an amplitude of  $0.05\Delta u$ . Random noise with an amplitude of  $\pm 0.005\Delta u$  was also added. This perturbation method is identical to that of Carpenter *et al.*,<sup>57</sup> triggering the rapid growth of Holmboe waves.

The two-dimensional multiple wavelength simulation was initialized with random noise in the velocity field to stimulate the growth of

the instabilities and allow different wavenumbers to evolve initially. The amplitude of the perturbation is uniformly distributed in the range  $\pm 0.05\Delta u$ . A simple sinusoidal perturbation was also added to the density interface with the initial wavenumber of maximum growth ( $k_{\text{initial}}$ ) and an amplitude of  $0.05\Delta u$ . A summary of the simulations is shown in Table I. Unless explicitly stated, we will refer to the two-dimensional single wavelength simulation (two-dimensional multiple wavelength simulation) simply as single wavelength simulation (multiple wavelength simulation) hereafter.

#### A. Single wavelength simulations

##### 1. Counter-propagating Holmboe waves

Counter-propagating Holmboe waves vary between an “anti-phase” state ( $\phi = 0$ ) and an “in phase” state ( $\phi = \pi$ ), as in standing waves. Figure 3 is a plot of  $u'$  for (a)  $\phi = 0$  and (b)  $\phi = \pi$ . When the two waves are in antiphase ( $\phi = 0$ ), the density interface is nearly horizontal, and the velocity perturbations are of maximum amplitude. While the two waves are in phase ( $\phi = \pi$ ), the deflection of the density interface is the greatest and the corresponding velocity perturbations are minimal. The velocity and density perturbations do not vanish completely at any phase.

##### 2. Comparison between numerical simulations and linear stability analysis

To compare the Reynolds stress in numerical simulations with linear theory, we separate the flow field associated with the rightward and leftward propagating modes by performing two-dimensional Fourier transforms of the velocity perturbation fields at each vertical level, similar to that of the wave field in Tedford *et al.*<sup>24</sup> Figure 2 shows the evolution of horizontally averaged Reynolds stress  $\langle u'w' \rangle_x$  in the single wavelength simulation for the total field in panel (e), the leftward propagating mode in panel (f), and the rightward propagating mode in panel (g). Note that the total Reynolds stress oscillates, and its

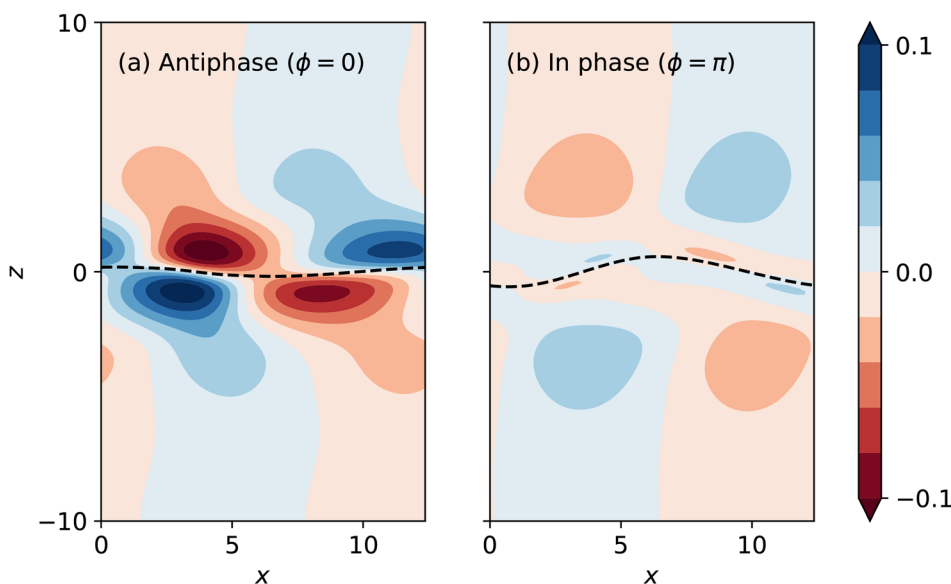


**FIG. 3.** Representative plots of the horizontal velocity perturbation,  $u'$ , in counter-propagating Holmboe waves for (a) antiphase ( $\phi = 0$ ,  $t = 76$ ) and (b) in phase ( $\phi = \pi$ ,  $t = 82$ ) in the single wavelength simulation. The dashed line is the density interface. Note that the magnitude of  $w'$  is similarly maximal at  $\phi = 0$  and minimal at  $\phi = \pi$ .

vertical extent and magnitude increase with time. As the two waves propagate in opposite directions, the frequency of the oscillation in this pattern is double that of the individual modes [see Eq. (19)].

Once the modes are separated with the Fourier transform, the oscillations disappear in both the leftward and rightward propagating modes [Figs. 2(f) and 2(g)]; only a growing pattern remains. The magnitude is mainly concentrated above (below) the density interface for the rightward (leftward) propagating mode. It can be seen that the superposition of the two modes produces an additional phase-dependent wave interaction field. This interaction field is shown in panel (h), obtained through the subtraction of (f) and (g) from (e). A nearly symmetric pattern of growth and decay is observed in each half-wave period.

Figures 4(a) and 4(b) are the comparison of the mean vertical Reynolds stress profiles for each mode between linear stability analysis and the single wavelength simulation within one wave period ( $t = 76 - 88$ ), normalized for direct comparison. Over one wave period in the simulation, the vertical diffusion of the background profiles is negligible for each mode. The peak value of Reynolds stress is located near  $z = 1$  ( $z = -1$ ) for the rightward (leftward) propagating mode. The horizontally averaged Reynolds stress,  $\langle u'w' \rangle_{x;R}$  or  $\langle u'w' \rangle_{x;L}$ , is generally independent of time (panel b). This independence is consistent with the linear stability analysis for an individual mode (panel a) illustrating that  $\langle u'w' \rangle_x = \langle u'w' \rangle_t = \langle u'w' \rangle_{xt}$  [see Eq. (20)].

The comparison of the total field between linear stability analysis and the single wavelength simulation is shown in Figs. 4(c) and 4(d). As expected, the profiles vary with time. The maximum amplitude appears at  $\phi = 0$  (antiphase), where the instability extracts energy most efficiently from the mean flow. While the small positive values at  $\phi = \pi$  (in phase) mean that Holmboe instability returns some energy back to the mean flow. On average over one period, the instability still extracts energy from the background mean flow. The vertical structure of the Reynolds stress from the simulation has the same form as that predicted by the linear stability theory.

## B. Multiple wavelength simulations

In the multiple wavelength simulation, we seeded a random initial perturbation (similar to Carpenter *et al.*<sup>19</sup>) because seeding an eigenfunction perturbation in the multiple wavelength simulation, as we did in the single wavelength simulation, simply copies the results of the single wavelength simulation over multiple wavelengths.

### 1. Wavenumber shifting

The density and vorticity fields for the multiple wavelength simulation are shown in Fig. 5. Starting with initial random perturbation at

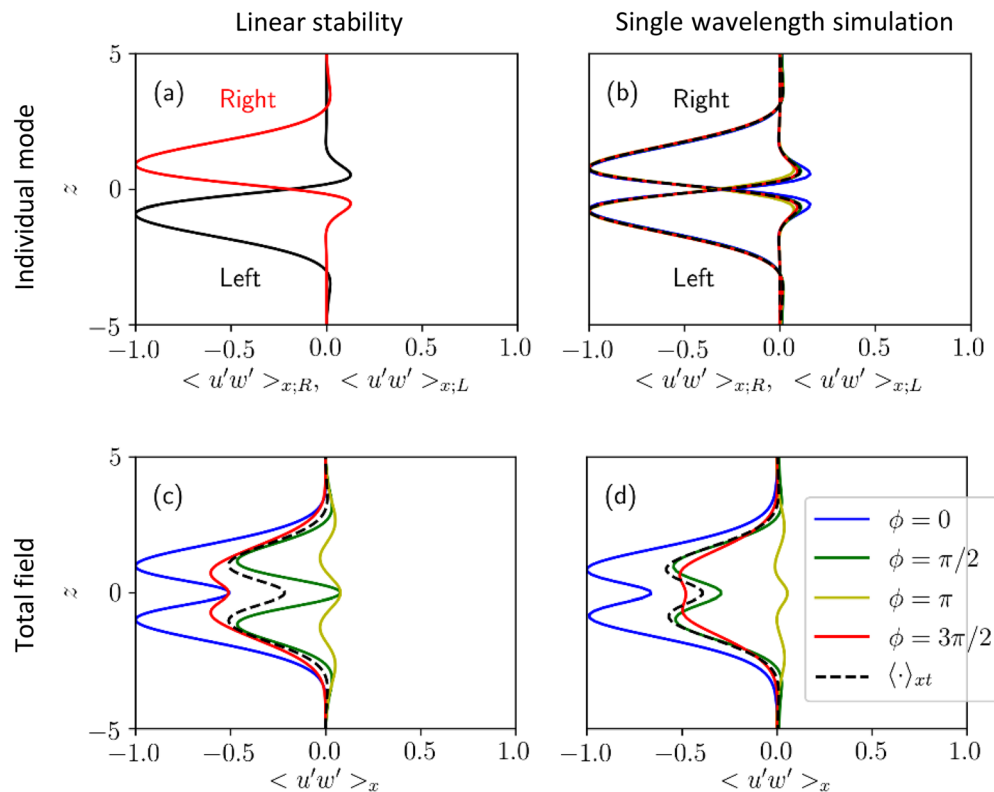


**FIG. 4.** Comparison of the normalized Reynolds stress between the linear stability analysis (the left column) and the single wavelength simulation (the right column) at different phases within a wave period. In linear stability analysis, four different phases with a  $\pi/2$  interval are selected as representative. The corresponding times in the simulation are  $t = 76$  ( $\phi = 0$ ),  $t = 79$  ( $\phi = \pi/2$ ),  $t = 82$  ( $\phi = \pi$ ), and  $t = 85$  ( $\phi = 3\pi/2$ ). Above the horizontal dashed line, (a) and (b) are the Reynolds stresses of individual modes, i.e., rightward and leftward propagating modes. Below the horizontal dashed line, (c) and (d) are the total Reynolds stresses;  $\langle \cdot \rangle_{xt}$  represents  $\langle u'w' \rangle_{xt}$ .

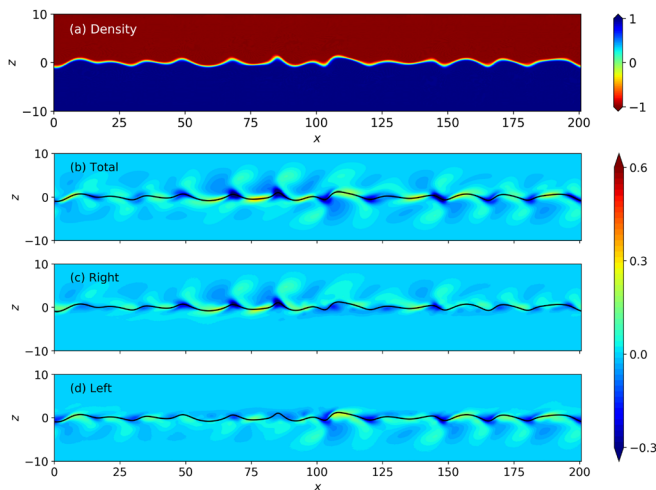


**FIG. 5.** Representative plots of the density fields (a) and perturbation vorticity field (b)–(d) at  $t = 220$  in the multiple wavelength simulation. (b)–(d) are the perturbation vorticity field for the total, rightward propagating, and leftward propagating wave modes, respectively. The black line represents the density interface.

$t = 0$ , energy is extracted from the mean flow by the instability and fed into the wave field at, or very close to, the initial wavenumber of maximum growth ( $k_{initial}$ ). This results in approximately 16 wavelengths in the computational domain at an early time. Eventually, the waves grow near the density interface, which can be seen in Fig. 5(a). The wave peaks (upward-pointing cusps) are propagating to the right, and the wave troughs (downward-pointing cusps) are propagating to the left. The corresponding perturbation vorticity of the total, rightward, and leftward wave fields are shown in panels (b)–(d) respectively. Similar to the direction of the cusps in the density field, the perturbation vorticities above (below) the density interface are associated with the rightward (leftward) propagating waves. At this time ( $t = 220$ ), 11 waves (fewer than the initial 16 waves) were observed, indicating that wave merging has occurred (discussed later in Sec. IV B 2). The leading vorticities associated with the rightward (panel c) and the leftward (panel d) propagating waves are irregularly spaced and of varying strength. As a result, it is not feasible to make a direct comparison of the horizontally averaged perturbation field as was shown in Fig. 4 for the single wavelength simulation.

## 2. Comparison of growth rate between single wavelength and multiple wavelength simulations

The evolution of the perturbation kinetic energy ( $\langle K' \rangle_{xz} = \langle u'^2 + w'^2 \rangle_{xz}/2$ ) for the single wavelength and multiple wavelength simulations is plotted in Fig. 6. After a startup period in which the energy of the initial perturbation rapidly decays, the waves grow. In the case of the single wavelength simulation [Fig. 6(a)], the averaged perturbation kinetic energy shows a strong oscillation throughout the whole simulation. This oscillation has a period of  $2\omega$  and is a result of energy exchange between the perturbation kinetic energy and perturbation potential energy<sup>58</sup> in the standing wave highlighted in Fig. 3. Once the leftward and rightward modes are separated and their individual kinetic energies linearly summed ( $\langle K' \rangle_{xz;R+L} = \langle K' \rangle_{xz;R} + \langle K' \rangle_{xz;L}$ ),

the oscillation is absent, similar to the Reynolds stress in Eq. (21). The perturbation kinetic energy for individual modes is approximately equal, i.e.,  $\langle K' \rangle_{xz;R} \approx \langle K' \rangle_{xz;L}$ . Accounting for the evolving background profiles, the kinetic energy for  $k_{initial}$  and  $k_{max}$  at each time step is estimated from linear stability theory, also shown in Fig. 6(a). Both the predicted growth rates continuously decrease due to the diffusion of the background flow over time. The growth rate of  $k_{max}$  overestimates the perturbation kinetic energy, while that of  $k_{initial} = 0.5$  successfully predicts the energy during the growth period since the observed wavenumber in the single wavelength simulation is fixed [observed  $k = k_{initial}$  in Fig. 6(c)]. Once the waves saturate ( $t > 160$ ), the linear prediction ( $k_{initial}$ ) begins to deviate from the simulation indicating the dominance of non-linear processes. During this non-linear period, the separation of the perturbation kinetic energy for the rightward and leftward propagating waves remains effective.

Unlike the strong oscillation in the averaged perturbation kinetic energy in the single wavelength simulation, the growth of perturbation kinetic energy in the multiple wavelength simulation is relatively steady [Fig. 6(b)]. This is due to the fact the leftward and rightward propagating waves have a distribution of phases and amplitudes in  $x$  at any given time (e.g., Fig. 5), resulting in less coherent interferences. Thus, the averaged kinetic energy is close to the linear summation of the rightward and leftward waves ( $\langle K' \rangle_{xz} \approx \langle K' \rangle_{xz;R+L}$ ) when  $t \gtrsim 55$ . Before  $t = 55$ , the two wave modes cannot be accurately separated by the Fourier transform due to the non-modal Holmboe instability.<sup>59</sup> Even during the modal development period ( $t \gtrsim 55$ ), the growth rate of perturbation kinetic energy in the multiple wavelength simulation cannot be directly compared with the linear stability analysis as the number of Holmboe waves (and thus the relevant choice of wavenumber) is evolving in time. The predicted growth rate from the linear stability analysis with the initial wavenumber ( $k_{initial} = 0.5$ ) and the wavenumber of maximum growth ( $k_{max}$ ) is also shown in Fig. 6(b). The perturbation kinetic energy in the multiple wavelength simulation evolves between these two predicted results. The wave merging in this simulation results in maximum kinetic energy that is larger than that in the single wavelength simulation. Additional simulations (not included) with horizontal domain lengths between  $L_x = \lambda_0$  and  $L_x = 32\lambda_0$  indicated that a domain longer than  $16\lambda_0$  was found to have a negligible influence on the saturation of perturbation kinetic energy.

The wave merging events are similar to those reported in Carpenter *et al.*<sup>19</sup> This process of losing waves results in an observed wavenumber that is continually shifted downward, resulting in a redistribution of energy. The merging events are due to vortex pairing as in numerical simulations of Kelvin–Helmholtz instabilities (e.g., Refs. 60–63) and were also documented in the Holmboe instability through laboratory experiments in Lawrence *et al.*<sup>20</sup>

The decreasing wavenumber of instabilities in the multiple wavelength simulation and linear stability theory is plotted in Fig. 6(d). Limited by the periodic boundary conditions, the observed wavelength in the simulation evolves in discrete steps. In contrast, the linear stability theory is not limited to steps as it is not constrained in the horizontal domain. The decrease in  $k_{max}$  in time is due to the increasing shear layer thickness that results from diffusion. This variation in wavenumber is then reflected back to the observed Holmboe waves.



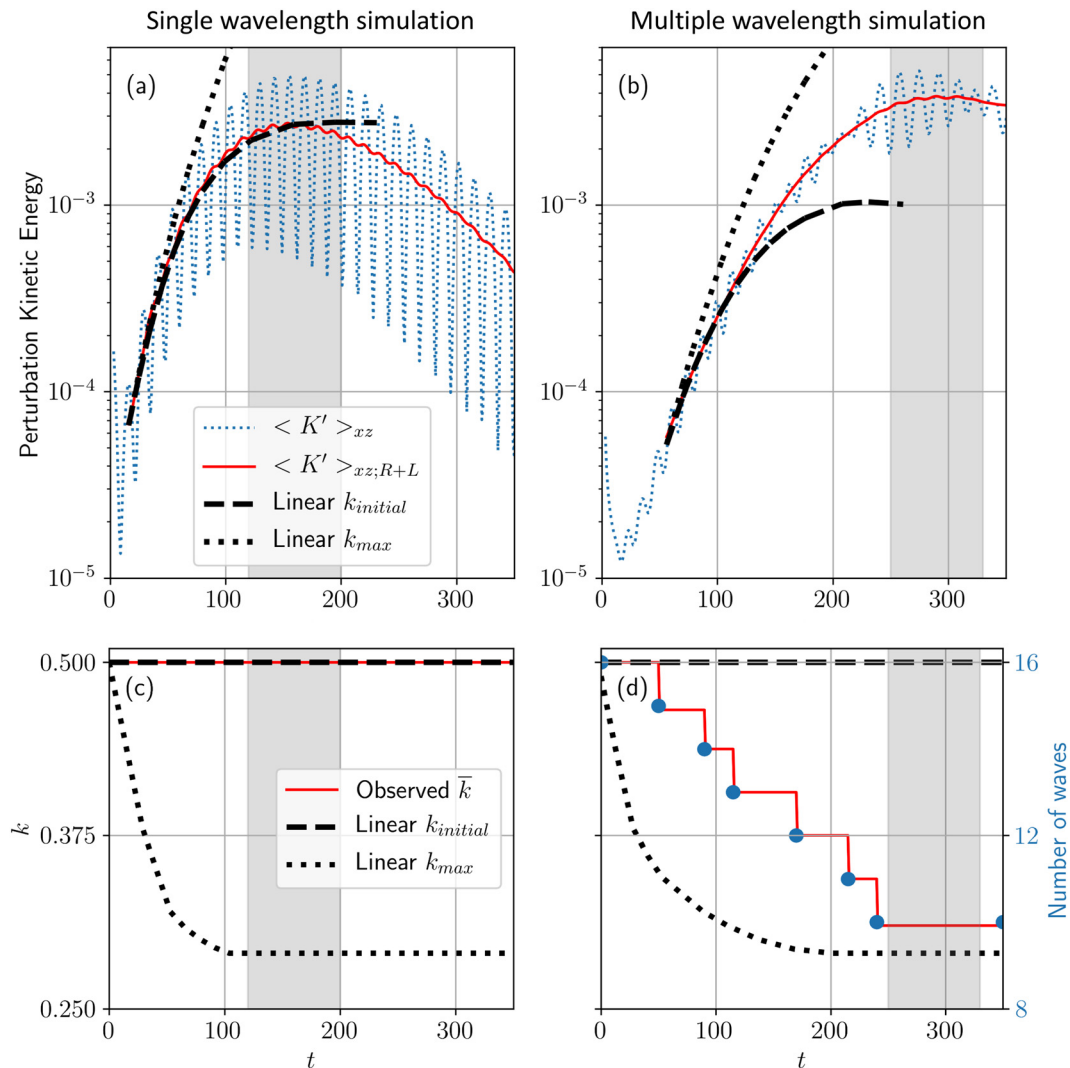


**FIG. 6.** Time evolution of the averaged perturbation kinetic energy ( $\langle K' \rangle_{xz}$ ) and wavenumber in the single wavelength simulation (the left column) and the multiple wavelength simulation (the right column). In (a) and (b), the red solid line is the linear summation of the averaged perturbation kinetic energy from the rightward and leftward propagating waves ( $\langle K' \rangle_{xz;R+L} = \langle K' \rangle_{xz;R} + \langle K' \rangle_{xz;L}$ ). The predicted growth rate from the linear stability analysis is denoted by the black dashed line ( $k_{initial} = 0.5$ ) and black dotted line ( $k_{max}$ ), which is a function of time owing to the changing background profiles. In (c) and (d), the black lines are from the same linear stability analysis and the red solid line is the observed average wavenumber in simulation with dots in (d) representing the number of waves evolving from the initial 16 waves ( $k = 0.5$ ) to 10 waves ( $k = 0.31$ ) in the multiple wavelength simulation. The shaded region is used for the analysis in Sec. V, where it is referred to as the quasi-steady period.

The growing mode in the simulation at every time step is not necessarily the “instantaneously” most unstable mode in linear stability analysis. Unlike the fixed wavenumber in the single wavelength simulation [Fig. 6(c)], the observed wavenumber in the multiple wavelength simulation is distributed between  $k_{initial}$  and  $k_{max}$ . Since the growth rate of the instability does not rely on a single wavenumber, its associated perturbation kinetic energy is distributed across  $k_{initial}$  (16 waves) to  $k = 0.31$  (final; 10 waves) over time. However, both the observed average wavenumber ( $\bar{k}$ ) and estimation ( $k_{max}$ ) approach a similar value of  $k = 0.31$  for  $t > 250$ . During this later period ( $t = 250$ – $330$ ), the perturbation kinetic energy is also relatively steady, hereafter referred to as the quasi-steady period (Table I).

## V. VARIANCE ELLIPSE AND REYNOLDS STRESS COMPARISONS

We compare  $(u', w')$  ellipses predicted using linear stability analysis with the probability density functions (PDFs) of  $(u', w')$  obtained using single wavelength and multiple wavelength simulations and those measured in laboratory experiment H3 of Lefauve *et al.*<sup>64,65</sup> The linear stability results are scaled for comparison with the simulation and laboratory results. For each comparison, we use the mean density and velocity profiles, and the observed wavenumber, during the quasi-steady period. In Sec. V A, we examine the  $(u', w')$  ellipses for the counter-propagating leftward and rightward waves, separately. The corresponding Reynolds stresses exhibit peaks on each side of the density interface (Fig. 7).

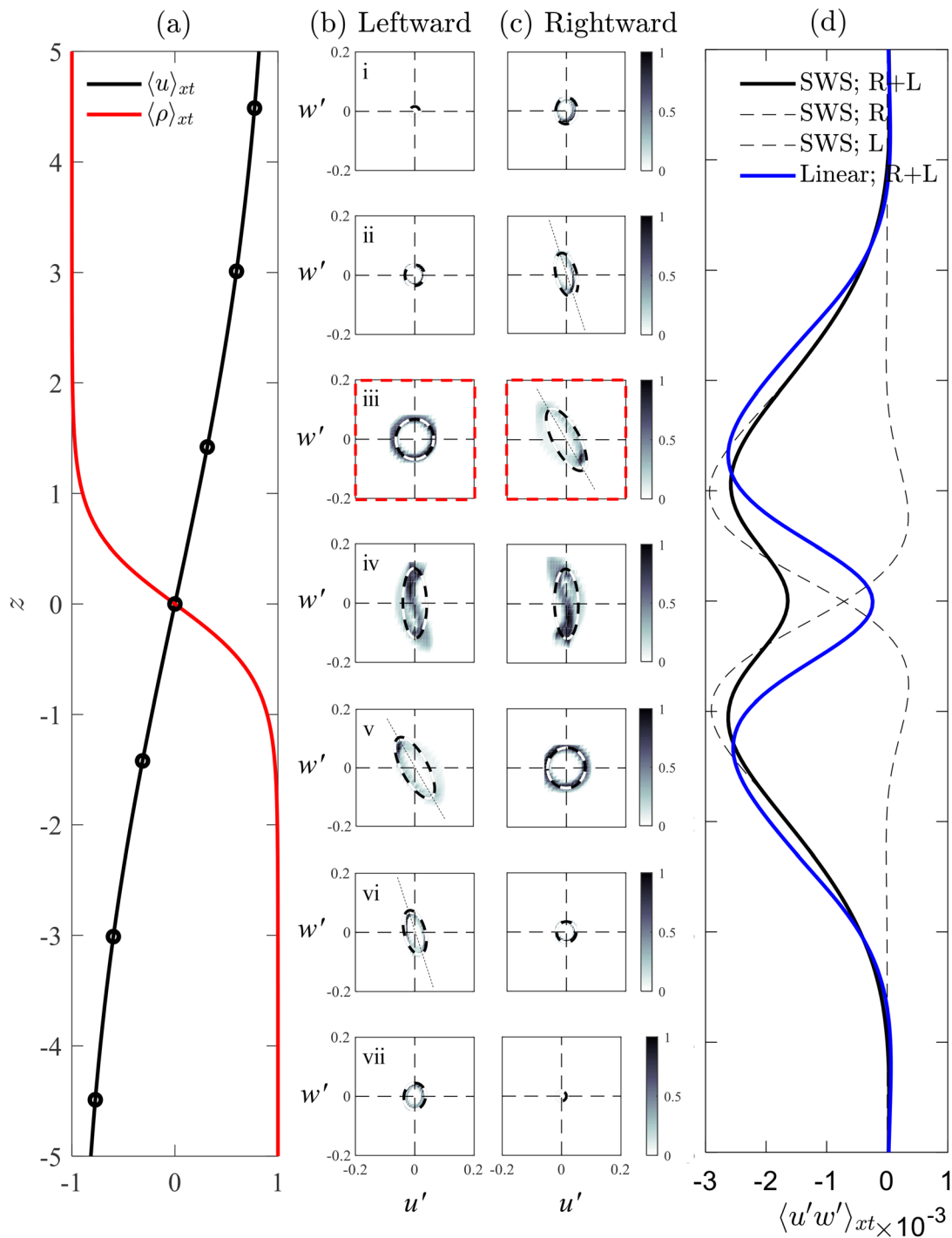


**FIG. 7.** Flow fields of the linear stability analysis and the single wavelength simulation (SWS) during the quasi-steady period. (a) Mean density and velocity profiles from the simulation. The black circles indicate the elevations of the  $(u', w')$ -pairs in (b) and (c). (b) and (c) are the comparisons of  $(u', w')$ -pairs between the linear stability analysis and the simulation for the leftward and rightward propagating modes, respectively. The  $(u', w')$ -pairs in the simulation are presented based on joint probability density functions (PDFs) where the darker color denotes the higher probability. The ellipses obtained from linear stability analysis are depicted using black–white lines, and their magnitudes are scaled with the simulation; their major axes are illustrated by dotted lines. (d) is the Reynolds stress. The  $(u', w')$ -pairs tilt toward the second and fourth quadrants within the shear layer below (above) and the density interface for the leftward (rightward) mode. The superposition of  $(u', w')$ -pairs within the red boxes (iii. at  $z = 1.4$ ) is presented in Figs. 8(a)–8(c).

In Sec. VB, the  $(u', w')$  ellipses due to the superposition of the counter-propagating waves at the vertical level of the peak Reynolds stress are examined (Fig. 8).

### A. Separated counter-propagating waves

The  $(u', w')$ -pairs for the leftward and rightward propagating waves, obtained from linear stability analysis, are compared with the single wavelength simulation during the quasi-steady period, in Figs. 7(b) and 7(c). In the linear stability analysis, the  $(u', w')$ -pairs form either circles or ellipses. Within the shear layer below the density interface, the  $(u', w')$ -pairs associated with the leftward propagating waves form ellipses that are oriented toward the second and fourth quadrants [Fig. 7(b)], and the corresponding Reynolds stresses are negative [Fig. 7(d)]. Above the density interface, the  $(u', w')$ -pairs associated with the leftward propagating waves form circles and do not contribute to the Reynolds stress. The  $(u', w')$ -pairs for the rightward propagating waves mirror those of the leftward propagating waves [Fig. 7(c)], as do their Reynolds stresses [Fig. 7(d)]. The joint PDFs of the  $(u', w')$ -pairs obtained in the simulation appear as “donut”-shaped clouds that, in general, closely match the ellipses and circles predicted using linear stability analysis [Figs. 7(b) and 7(c)]. However, deviations occur near  $z = 0$  due to non-linear interactions between the leftward and rightward propagating waves [panel (iv) in Figs. 7(b) and 7(c)]. The counter-propagating vorticity waves modeled by Tamarin *et al.*<sup>40</sup> exhibit similar features.

The vertical profiles of Reynolds stress have the same basic shape in both the single wavelength simulation and the linear stability analysis [Fig. 7(d)]. The profiles are symmetric about  $z = 0$ , with a minimum at  $z = 0$  and peaks at  $z \approx \pm 1.4$ , beyond, which the Reynolds stresses asymptote to zero. The peak above (below) the interface is due to the rightward (leftward) propagating wave. The vertical profiles of the Reynolds stress in both the multiple wavelength simulation and the laboratory experiment also exhibit the same basic shape as the single wavelength simulation and the linear stability prediction with peaks at  $z \approx \pm 1.6$  in the multiple wavelength simulation and  $z \approx 0.6$  in the laboratory experiment (see Appendix A). The peaks occur at different locations due to different mean velocity and density profiles.

### B. Superposed counter-propagating waves

In Figs. 7(b) and 7(c), we presented the  $(u', w')$  ellipses predicted by linear stability theory separately for the leftward and rightward propagating waves in the two-dimensional (2D) single wavelength simulation; when these  $(u', w')$  ellipses are added together, the orientation and aspect ratio of the resulting ellipses are phase-dependent, as shown in Fig. 8(a) for the 2D single wavelength simulation [Fig. 8(d) for the three-dimensional (3D) single wavelength simulation, Fig. 8(g) for the multiple wavelength simulation, Fig. 8(j) for the experiment]. At  $\phi = 0, \pi/2$ , and  $3\pi/2$ , the major axes of the  $(u', w')$  ellipses tilt toward the second and fourth quadrants, resulting in negative Reynolds stresses ( $\langle u'w' \rangle_x < 0$ ); while at  $\phi = \pi$ , the  $(u', w')$  ellipses tilt toward the 1st and 3rd quadrants, resulting in positive Reynolds stresses ( $\langle u'w' \rangle_x > 0$ ). These phase-dependent  $(u', w')$  ellipses due to the counter-propagating waves are expressed in detail in Appendix B, and similar results of the phase-dependent Reynolds stresses are shown in Figs. 2(a) and 4(c).

When the  $(u', w')$  ellipses of the counter-propagating waves are integrated over a full-wave period, the joint PDF of  $(u', w')$  is topologically similar to a four-spoked steering wheel as shown in Fig. 8(b) for the 2D single wavelength simulation [Fig. 8(e) for the 3D single wavelength simulation, Fig. 8(h) for the multiple wavelength simulation, and Fig. 8(k) for the experiment]. The vertices (along major axes) of these  $(u', w')$  ellipses combine to form the outer rim of the steering wheel since more data points are concentrated near these vertices, whereas the co-vertices (along minor axes) combine to form the spokes and hub of the steering wheel. The formation of the steering wheel structure due to multiple phases is described in Appendix B. The corresponding PDF of  $(u', w')$  from the 2D single wavelength simulation is shown in Fig. 8(c). While somewhat distorted, the tilted elliptical shape with steering wheel features is still apparent and similar to the linear stability predictions. The differences between them are presumably due to the slow growth and decay of instabilities during the quasi-steady period. The results obtained from the 2D single wavelength simulation are almost indistinguishable from the 3D single wavelength simulation [Figs. 8(d)–8(f)]. Note that the linear stability analysis is 2D in both Figs. 8(a) and 8(d) but based on slightly different background profiles due to slightly different conditions during the quasi-steady period in 2D the simulation compared to the 3D simulation.

To quantitatively compare the variance ellipses between the linear stability analysis and simulations, we calculate the tilt angle ( $\theta$ ), the ellipse anisotropy ( $a$ ), and the ellipse shape parameter ( $A$ ) as<sup>37</sup>

$$\theta = \frac{1}{2} \arctan \left( \frac{2\langle u'w' \rangle}{\langle u'u' - w'w' \rangle} \right), \quad (22a)$$

$$a = \frac{1}{2} (L_a^2 - L_b^2) = \sqrt{\langle u'u' - w'w' \rangle^2 + 4\langle u'w' \rangle^2}, \quad (22b)$$

$$A = \frac{L_a^2 - L_b^2}{L_a^2 + L_b^2} = \frac{\sqrt{\langle u'u' - w'w' \rangle^2 + 4\langle u'w' \rangle^2}}{\langle u'u' + w'w' \rangle}, \quad (22c)$$

where  $\langle \cdot \rangle$  represents the ensemble average;  $L_a$  and  $L_b$  are respectively the length of semi-major and semi-minor axes; and  $A$  varies between 0 (circle) and 1 (straight line). Based on the geometric parameters of the ellipse in Eqs. (22a) and (22b), the resulting Reynolds stress can be written as

$$\langle u'w' \rangle = -\frac{a |\tan(2\theta)|}{\sqrt{1 + [\tan(2\theta)]^2}}. \quad (23)$$

Although the PDF from the 2D single wavelength simulation is distorted, the geometric parameters of the variance ellipse are close to those predicted by the linear stability analysis [Figs. 8(b) and 8(c)]. The predicted tilt angle ( $\theta$ ) and ellipse shape parameter ( $A$ ), respectively, is 3% smaller and 10% larger than that in the simulation; as a result, the predicted Reynolds stress is 8% larger than that in the simulation. The geometric parameters obtained from the 3D single wavelength simulation are all the same to within 5% of values obtained from the 2D simulation [Figs. 8(e) and 8(f)].

The linear stability predictions from the multiple wavelength simulation are very similar to those of the single wavelength simulation [Figs. 8(g) and 8(h)] with minor differences attributable to the slightly broader velocity and density profiles during the quasi-steady

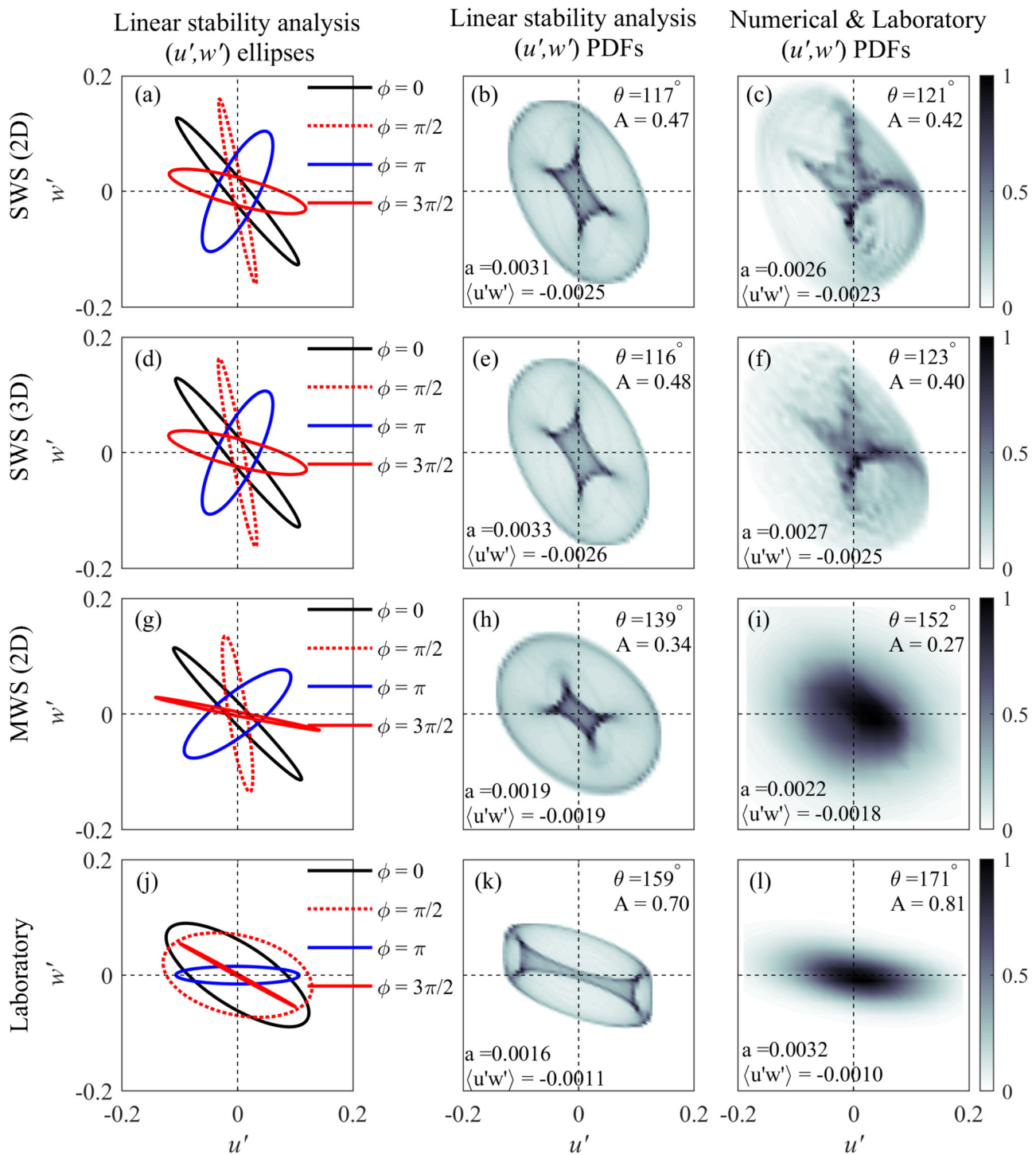


**FIG. 8.** The  $(u', w')$ -pairs of the superposition of the leftward and rightward propagating waves at the vertical level of the peak Reynolds stress for (a)–(c) 2D single wavelength simulation (SWS; the red box at  $z = 1.4$  in Fig. 7); (d)–(f) 3D SWS ( $z = 1.4$ ); (g)–(i) multiple wavelength simulation (MWS;  $z = 1.6$ ); and (j)–(l) the laboratory experiment of Lefauve *et al.*<sup>64</sup> ( $z = 0.6$ ). The  $(u', w')$  ellipses obtained from linear stability analysis for  $\phi = 0, \pi/2, \pi$ , and  $3\pi/2$  are presented in the left column (a), (d), (g), and (j). The probability density functions (PDFs) of  $(u', w')$  for a full-wave period are presented in the middle column (b), (e), (h), and (k). The PDFs for the 2D SWS, 3D SWS, MWS, and experiment are presented in the right column (c), (f), (i), and (l). The geometric parameters ( $\theta$ ,  $A$ , and  $a$ ) of  $(u', w')$  ellipses and the resultant Reynolds stresses ( $\langle u'w' \rangle$ ) are shown in the middle and right columns. The presence of multiple wavenumbers in the MWS and laboratory experiment results in solid cloud-like  $(u', w')$  ellipses.



period. However, the PDF of  $(u', w')$  forms a unimodal cloud in the multiple wavelength simulation, rather than the steering wheel pattern found in the single wavelength simulation [Fig. 8(c)] and the linear stability prediction [Fig. 8(h)]. This unimodal cloud reflects the complicated interactions between multiple counter-propagating waves of varying phases, amplitudes, and wavelengths in the multiple wavelength simulation [Fig. 8(i)]. Nevertheless, the cloud has a similar orientation and anisotropy as the steering wheel pattern predicted by linear stability theory; the resultant Reynolds stress values are also similar with a 5% difference.

Qualitatively, the linear stability predictions for the laboratory experiments are similar to those of single wavelength and multiple wavelength simulations [Figs. 8(j) and 8(k)]. However, the orientation and shape of the  $(u', w')$  ellipses are different. This is not surprising since the background mean velocity profiles in the laboratory experiment are nearly sinusoidal due to the no-slip condition at the top and bottom channel walls, as opposed to the hyperbolic tangent profiles in the single wavelength and multiple wavelength simulations. The joint PDF of  $(u', w')$  in the laboratory experiment is similar to the unimodal structure of the multiple wavelength simulation, due to the coexistence of multiple Holmboe wavelengths [Fig. 8(i)]. This PDF cloud resembles those characteristics of fully turbulent fields.<sup>34</sup> It also shows a comparable orientation and shape of ellipses as predicted from linear stability theory. The Reynolds stress predicted by linear stability analysis is marginally higher than that obtained from the laboratory measurements.

Although the values of the Reynolds stress presented in Fig. 8 were obtained at moderate Reynolds numbers, it is worth noting that they are consistent with those obtained in previous studies of much higher Reynolds number flows. Dick and Marsalek<sup>66</sup> estimated  $\langle u'w' \rangle = 1.4 \times 10^{-3}$  ( $\pm 20\%$ ) from the measured interface height along the Burlington Ship canal that connects Lake Ontario with Hamilton Harbor. Also in the Burlington Ship canal, Lawrence *et al.*<sup>67</sup> estimated  $\langle u'w' \rangle = 2 \times 10^{-3}$  ( $\pm 50\%$ ) from Acoustic Doppler current profiler measurements. These values all lie within the range of estimates compiled by Arita and Jirka<sup>68</sup> from previous laboratory and field studies.

## VI. SUMMARY AND CONCLUSIONS

We have investigated the velocity perturbations and resulting Reynolds stress generated by finite-amplitude Holmboe instabilities in stratified shear flows at moderate Reynolds numbers. Linear stability analysis was used to explain the initiation of Reynolds stresses by the interaction of counter-propagating Holmboe waves. Then, single wavelength and multiple wavelength simulations were used to study the effects of wavenumber shifting on the instabilities from linear growth to saturation and the influence of the presence of multiple wavelengths on velocity perturbations and Reynolds stresses.

Linear stability analysis predicts that the  $(u', w')$ -pairs associated with the leftward (rightward) propagating waves form ellipses within the shear layer below (above) the density interface. These ellipses are orientated toward the second and fourth quadrants, corresponding to the tilted elliptical trajectories of particle orbits in Holmboe waves. Combining the leftward and rightward modes yields  $(u', w')$  ellipses whose orientation and aspect ratio are dependent on the phase of the counter-propagating waves. The corresponding joint PDFs of  $(u', w')$  over a full-wave period exhibit a steering wheel structure.

In the single wavelength simulation, the joint PDFs of  $(u', w')$  for the rightward and the leftward propagating waves are donut shaped ellipses, which closely match the ellipses predicted using linear stability analysis. When the leftward and rightward modes are combined, the joint PDF of  $(u', w')$  yields a steering wheel structure similar to that predicted by linear theory. In the multiple wavelength simulation and laboratory experiment, the presence of multiple waves with varying wavelengths, phases, and amplitudes smears out the steering wheel structure, leaving an elliptical cloud with similar orientation and shape to the corresponding linear prediction.

The  $(u', w')$  ellipses obtained from the linear stability analysis, numerical simulations, and the laboratory experiment are all predominantly oriented toward the second and fourth quadrants, resulting in negative Reynolds stresses within the shear layer. The vertical profile of the Reynolds stresses exhibits two peaks, above and below the density interface. The upper and lower peaks are respectively caused by the rightward and leftward propagating Holmboe waves. The magnitude of Reynolds stresses obtained in the present study is consistent with those reported in previous laboratory and field investigations.<sup>66–68</sup>

The present work examines the velocity perturbations and Reynolds stresses associated with the finite-amplitude Holmboe instability in unforced numerical simulations. These simulations were compared with the forced (tilted tube) laboratory experiment of Lefauve *et al.*<sup>50</sup> Future research using forced numerical simulations, similar to those of Smith *et al.*,<sup>6</sup> could allow a closer comparison with laboratory experiments. The present study has only considered a single point in the Holmboe instability parameter space; results will differ at different values of  $Re$ ,  $J$ ,  $Sc$ , and  $R$ . At higher  $Re$  ( $10^3$ – $10^4$ ), Salehipour *et al.*<sup>5</sup> showed that the shear-aligned secondary convective instability can play a crucial role in three-dimensionalization of the flow. Further study is needed to examine how the nature of the Reynolds stress changes as the Reynolds number changes. Also, we have limited our investigation to the classical symmetric Holmboe instability where the density interface is coincident with the center of the shear layer. This is a special case of a more general situation in which the center of the sheared and stratified layers may be offset from one another.<sup>20,57</sup> If the offset is sufficiently large, only one of the two Holmboe modes will occur. A more comprehensive study would investigate this offset as well as additional points in  $Re$ ,  $J$ ,  $Sc$ , and  $R$  parameter space.

## ACKNOWLEDGMENTS

This study was supported by the Natural Sciences and Engineering Research Council of Canada. A.L. was supported by the Leverhulme Trust Early Career Fellowship.

## AUTHOR DECLARATIONS

### Conflict of Interest

The authors have no conflicts to disclose.

## Author Contributions

**Adam J. K. Yang:** Data curation (equal); Formal analysis (equal); Investigation (equal); Methodology (equal); Writing – original draft (equal); Writing – review and editing (equal). **E. W. Tedford:** Data curation (supporting); Formal analysis (supporting); Investigation



(supporting); Methodology (supporting); Writing – original draft (supporting); Writing – review and editing (supporting). **J. Olsthoorn:** Data curation (supporting); Formal analysis (supporting); Investigation (supporting); Methodology (supporting); Writing – original draft (supporting); Writing – review and editing (supporting). **A. Lefauve:** Data curation (supporting); Formal analysis (supporting); Investigation (supporting); Writing – review and editing (supporting). **G. A. Lawrence:** Data curation (supporting); Formal analysis (supporting); Funding acquisition (lead); Investigation (supporting); Methodology (supporting); Supervision (lead); Writing – original draft (supporting); Writing – review and editing (supporting).

## DATA AVAILABILITY

The data that support the findings of this study are available from the corresponding author upon reasonable request.

## APPENDIX A: REYNOLDS STRESS PROFILES IN THE MULTIPLE WAVELENGTH SIMULATION AND LABORATORY

The vertical profiles of the Reynolds stress in the multiple wavelength simulation and laboratory experiment are similar to those predicted by the linear stability analysis (Fig. 9). As in the single wavelength simulation, both the multiple wavelength simulation and laboratory experiment exhibit two peaks in the vertical profile, one above and one below the density interface. A slight asymmetry in the Reynolds stress profiles for the laboratory experiment results from the experimental configuration, which leads to slightly stronger vorticity above the interface than below the interface.<sup>50,64</sup> This slight asymmetry is also captured by the linear stability analysis. There is also a region of positive Reynolds stress near the upper and lower boundaries in the laboratory experiment, which again is likely due to the irregular nature of the velocity profile.

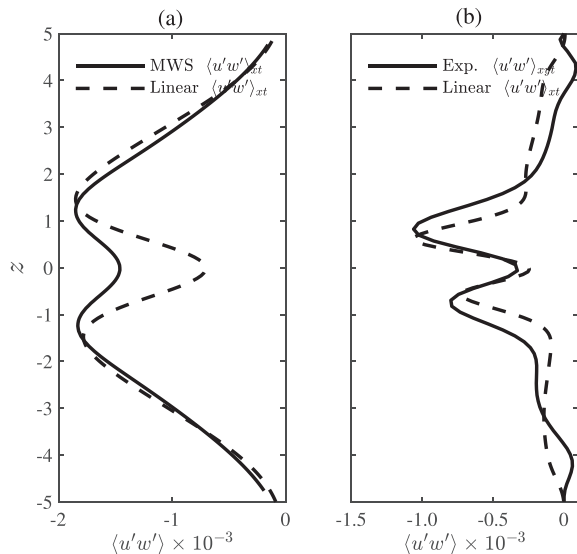


**FIG. 9.** Comparison of the vertical profiles of the Reynolds stress between the linear stability analysis and (a) the multiple wavelength simulation and (b) the laboratory experiment.

## APPENDIX B: EFFECT OF PHASE ON THE SUPERIMPOSED VELOCITY PERTURBATION PAIRS

Following the normal mode assumption, the velocity perturbations for the leftward propagating wave at the vertical level,  $z_0$ , are expressed as

$$u^{(L)}(x, z_0, t) \equiv \frac{1}{2} \left[ \hat{u}^{(L)}(z_0) e^{i(k_L x - \omega_L t)} + c.c. \right], \quad (B1a)$$

$$w^{(L)}(x, z_0, t) \equiv \frac{1}{2} \left[ \hat{w}^{(L)}(z_0) e^{i(k_L x - \omega_L t)} + c.c. \right], \quad (B1b)$$

where  $\hat{u}^{(L)}(\hat{w}^{(L)})$  at one vertical level is a complex constant and denoted by  $\hat{u}^{(L)}(z_0) = a_L + ib_L$  and  $\hat{w}^{(L)}(z_0) = c_L + id_L$ . The constants ( $a_L, b_L, c_L, d_L \in \mathbb{R}$ ) are obtained by numerically solving the T-G equation with the background mean velocity and density profiles. Then, the velocity perturbations for the leftward propagating wave can be rewritten as

$$u^{(L)}(x, z_0, t) = a_L \cos(k_L x - \omega_L t) - b_L \sin(k_L x - \omega_L t), \quad (B2a)$$

$$w^{(L)}(x, z_0, t) = c_L \cos(k_L x - \omega_L t) - d_L \sin(k_L x - \omega_L t). \quad (B2b)$$

Noting  $\theta_L(x, t) = k_L x - \omega_L t$ , we rewrite  $u^{(L)}$  as

$$u^{(L)}(x, z_0, t) = a_L \cos \theta_L - b_L \sin \theta_L = \sqrt{a_L^2 + b_L^2} \sin(\alpha_{uL0} + \theta_L), \quad (B3)$$

where  $\alpha_{uL0} = \tan^{-1}[-\frac{a_L}{b_L}]$ . Similarly, the vertical velocity perturbation at  $z_0$  is

$$w^{(L)}(x, z_0, t) = \sqrt{c_L^2 + d_L^2} \sin(\alpha_{wL0} + \theta_L), \quad (B4)$$

where  $\alpha_{wL0} = \tan^{-1}[-\frac{c_L}{d_L}]$ .

Applying the same procedures, the horizontal and vertical velocity perturbations for the rightward propagating wave at  $z_0$  are expressed as

$$u^{(R)}(x, z_0, t) = \sqrt{a_R^2 + b_R^2} \sin(\alpha_{uR0} + \theta_R), \quad (B5a)$$

$$w^{(R)}(x, z_0, t) = \sqrt{c_R^2 + d_R^2} \sin(\alpha_{wR0} + \theta_R), \quad (B5b)$$

where the constants ( $a_R, b_R, c_R, d_R \in \mathbb{R}$ ) are obtained from the eigenfunction of the rightward propagating wave, i.e.,  $\hat{u}^{(R)}(z_0) = a_R + ib_R$ ,  $\hat{w}^{(R)}(z_0) = c_R + id_R$ ;  $\alpha_{uR0} = \tan^{-1}[-\frac{a_R}{b_R}]$ ;  $\alpha_{wR0} = \tan^{-1}[-\frac{c_R}{d_R}]$ ; and  $\theta_R(x, t) = k_R x - \omega_R t$ .

For an individual wave, the horizontal and vertical velocity perturbations are in phase. The temporal and spatial variations are expressed by the term  $\theta_L$  ( $\theta_R$ ) for the leftward (rightward) propagating wave, thus varying over either one wavelength or one wave period yields the same result. The  $(u', w')$  ellipses for the leftward and rightward propagating modes, at the vertical level of the peak Reynolds stress ( $z_0 = 1.4$ ) for example, are shown in the red box in Figs. 7(b) and 7(c), respectively. It can be seen that the orientation and aspect ratio of the ellipses depend on the constants  $a_L, b_L, c_L$ , and  $d_L$  ( $a_R, b_R, c_R$ , and  $d_R$ ) for the leftward (rightward) propagating wave. Note that these constants depend on background mean velocity and density profiles.

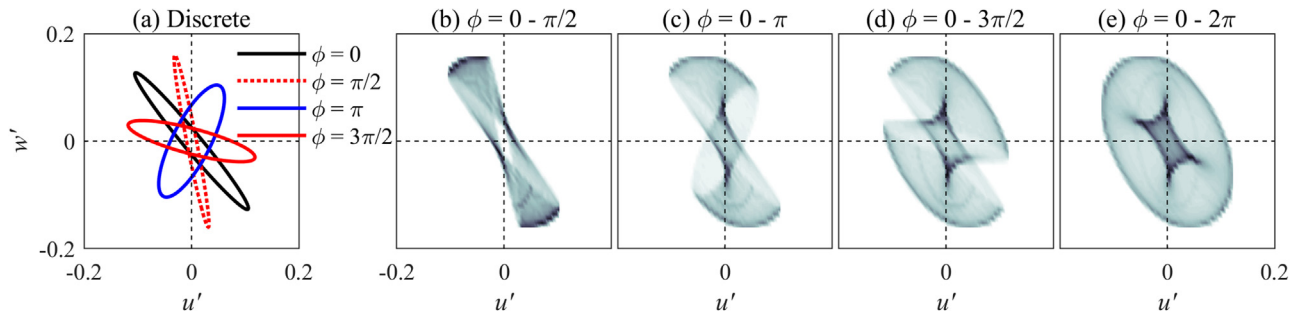


**FIG. 10.** The influence of phase ( $\phi$ ) on  $(u', w')$ -pairs at  $z_0 = 1.4$ : (a) discrete  $\phi = 0, \phi = \pi/2, \phi = \pi$ , and  $\phi = 3\pi/2$ , (b) the PDF of  $\phi = 0 - \pi/2$ , (c) the PDF of  $\phi = 0 - \pi$ , (d) the PDF of  $\phi = 0 - 3\pi/2$ , and (e) the PDF of  $\phi = 0 - 2\pi$ . In (b)–(e), the darker color denotes the higher probability.

Now, we examine the superimposed velocity perturbation pairs by the counter-propagating Holmboe waves. Based on Eqs. (B3), (B4), (B5a), and (B5b), the superimposed velocity perturbations are expressed as

$$u'(x, z_0, t) = u'^{(L)} + u'^{(R)} \\ = \sqrt{a_L^2 + b_L^2} \sin(\alpha_{uL0} + \theta_L) + \sqrt{a_R^2 + b_R^2} \sin(\alpha_{uR0} + \theta_R), \quad (\text{B6a})$$

$$w'(x, z_0, t) = w'^{(L)} + w'^{(R)} \\ = \sqrt{c_L^2 + d_L^2} \sin(\alpha_{wL0} + \theta_L) + \sqrt{c_R^2 + d_R^2} \sin(\alpha_{wR0} + \theta_R). \quad (\text{B6b})$$

The superimposed velocity perturbations contain the contribution from leftward and rightward propagating waves in  $\theta_L = k_L x - \omega_L t$  and  $\theta_R = k_R x - \omega_R t$ , respectively. For symmetric Holmboe waves, we have  $k_L = k_R = k$  and  $\omega_L = -\omega_R = \omega$ . The superimposed velocity perturbations can be expressed as

$$u' = \sqrt{a_L^2 + b_L^2} \sin(\alpha_{uL0} + kx - \phi/2) \\ + \sqrt{a_R^2 + b_R^2} \sin(\alpha_{uR0} + kx + \phi/2), \quad (\text{B7a})$$

$$w' = \sqrt{c_L^2 + d_L^2} \sin(\alpha_{wL0} + kx - \phi/2) \\ + \sqrt{c_R^2 + d_R^2} \sin(\alpha_{wR0} + kx + \phi/2), \quad (\text{B7b})$$

where  $\phi = 2\omega t$  is the phase between the leftward and rightward propagating waves. When  $\phi = 0$ , the superposition of counter-propagating waves results in a density interface that is nearly horizontal [Fig. 3(a)]. When  $\phi = \pi$ , the resultant deflection of the density interface is maximum [Fig. 3(b)]. For multiple values of phase  $\phi$ ,  $kx$  spanning over one wavelength yields different ellipses with different aspect ratios and orientations as shown in Fig. 10(a). The steering wheel structure in Fig. 8(b) is formed due to different phases of the counter-propagating Holmboe waves. The intermediate steps forming this structure are illustrated in Fig. 10. When  $\phi = 0$ , the  $(u', w')$ -pairs form an ellipse, the major axis of which tilt toward the first and third quadrants. From  $\phi = 0$  to  $\phi = \pi/2$ , the aspect ratio and tilt angle of the  $(u', w')$  ellipses are continuously evolving within the first and third quadrants. The joint PDF of

$(u', w')$  integrated from  $\phi = 0$  to  $\phi = \pi/2$  is smeared and forms a shape with a higher probability at the edge and near the hub [Fig. 10(b)]. With progressively more phases included, the joint PDFs of  $(u', w')$  are shown in Figs. 10(c)–10(e). Eventually, when the  $(u', w')$  ellipses are integrated over a full-wave period, the joint PDF of  $(u', w')$  is topologically similar to a four-spoked steering wheel as shown in Fig. 8(b).

## REFERENCES

- <sup>1</sup>S. A. Thorpe, "Experiments on the instability of stratified shear flows: Miscible fluids," *J. Fluid Mech.* **46**, 299–319 (1971).
- <sup>2</sup>W. D. Smyth and J. N. Moum, "Ocean mixing by Kelvin-Helmholtz instability," *Oceanography* **25**, 140–149 (2012).
- <sup>3</sup>J. Holmboe, "On the behavior of symmetric waves in stratified shear layers," *Geophys. Publ.* **24**, 67–113 (1962).
- <sup>4</sup>F. K. Browand and C. D. Winant, "Laboratory observations of shear-layer instability in a stratified fluid," *Bound.-Layer Meteorol.* **5**, 67–77 (1973).
- <sup>5</sup>H. Salehpour, C. P. Caulfield, and W. R. Peltier, "Turbulent mixing due to the Holmboe wave instability at high Reynolds number," *J. Fluid Mech.* **803**, 591–621 (2016).
- <sup>6</sup>K. M. Smith, C. P. Caulfield, and J. R. Taylor, "Turbulence in forced stratified shear flows," *J. Fluid Mech.* **910**, A42 (2021).
- <sup>7</sup>A. K. Kaminski, E. A. D'Asaro, A. Y. Shcherbina, and R. R. Harcourt, "High-resolution observations of the North Pacific transition layer from a Lagrangian float," *J. Phys. Oceanogr.* **51**, 3163–3181 (2021).
- <sup>8</sup>H. van Haren, "Stratified turbulence and small-scale internal waves above deep-ocean topography," *Phys. Fluids* **25**, 106604 (2013).
- <sup>9</sup>R. Plougonven and F. Zhang, "Internal gravity waves from atmospheric jets and fronts," *Rev. Geophys.* **52**, 33–76, <https://doi.org/10.1002/2012RG000419> (2014).
- <sup>10</sup>E. W. Tedford, J. R. Carpenter, R. Pawlowicz, R. Pieters, and G. A. Lawrence, "Observation and analysis of shear instability in the Fraser River estuary," *J. Geophys. Res. Oceans* **114**, C11006, <https://doi.org/10.1029/2009JC005313> (2009).
- <sup>11</sup>N. C. Delpeche, T. Soomere, and M.-J. Lilover, "Diapycnal mixing and internal waves in the Saint John River Estuary, New Brunswick, Canada with a discussion relative to the Baltic Sea," *Est. J. Eng.* **16**, 157 (2010).
- <sup>12</sup>P. Held, K. Bartholomä-Schrottke, and A. Bartholomä, "Indications for the transition of Kelvin-Helmholtz instabilities into propagating internal waves in a high turbid estuary and their effect on the stratification stability," *Geo-Mar. Lett.* **39**, 149–159 (2019).
- <sup>13</sup>S. Yoshida, M. Ohtani, S. Nishida, and P. F. Linden, "Mixing processes in a highly stratified river," *Coastal and Estuarine Studies*, Vol. 54 389–400 (1998).
- <sup>14</sup>G. A. Douillet, Q. Chaffaut, F. Schlunegger, U. Kueppers, and D. B. Dingwell, "Shark-fins: Overturned patterns linked to shear instabilities at the flow-bed boundary. Examples from the deposits of the 2006 pyroclastic currents at Tungurahua volcano (Ecuador)," *EarthArXiv* (2018).
- <sup>15</sup>W. D. Smyth and K. B. Winters, "Turbulence and mixing in Holmboe waves," *J. Phys. Oceanogr.* **33**, 694–711 (2003).

- <sup>16</sup>A. J. K. Yang, E. W. Tedford, and G. A. Lawrence, "The spatial evolution of velocity and density profiles in an arrested salt wedge," *Theor. Appl. Mech. Lett.* **9**, 403–408 (2019).
- <sup>17</sup>C. Wunsch and R. Ferrari, "Vertical mixing, energy, and the general circulation of the oceans," *Annu. Rev. Fluid Mech.* **36**, 281–314 (2004).
- <sup>18</sup>M. C. Gregg, E. A. D'Asaro, J. J. Riley, and E. Kunze, "Mixing efficiency in the ocean," *Annu. Rev. Mar. Sci.* **10**, 443–473 (2018).
- <sup>19</sup>J. R. Carpenter, E. W. Tedford, M. Rahmani, and G. A. Lawrence, "Holmboe wave fields in simulation and experiment," *J. Fluid Mech.* **648**, 205–223 (2010).
- <sup>20</sup>G. A. Lawrence, F. K. Browand, and L. G. Redekopp, "The stability of a sheared density interface," *Phys. Fluids A* **3**, 2360–2370 (1991).
- <sup>21</sup>O. Pouliquen, J. M. Chomaz, and P. Huerre, "Propagating Holmboe waves at the interface between two immiscible fluids," *J. Fluid Mech.* **266**, 277–302 (1994).
- <sup>22</sup>D. Z. Zhu and G. A. Lawrence, "Holmboe's instability in exchange flows," *J. Fluid Mech.* **429**, 391–409 (2001).
- <sup>23</sup>A. M. Hogg and G. N. Ivey, "The Kelvin-Helmholtz to Holmboe instability transition in stratified exchange flows," *J. Fluid Mech.* **477**, 339–362 (2003).
- <sup>24</sup>E. W. Tedford, R. Pieters, and G. A. Lawrence, "Symmetric Holmboe instabilities in a laboratory exchange flow," *J. Fluid Mech.* **636**, 137–153 (2009).
- <sup>25</sup>A. J. K. Yang, E. W. Tedford, J. Olsthoorn, and G. A. Lawrence, "Asymmetric Holmboe instabilities in arrested salt-wedge flows," *Phys. Fluids* **34**, 036601 (2022).
- <sup>26</sup>J. R. Carpenter, N. J. Balmforth, and G. A. Lawrence, "Identifying unstable modes in stratified shear layers," *Phys. Fluids* **22**, 054104 (2010).
- <sup>27</sup>J. R. Carpenter and A. Guha, "Instability of a smooth shear layer through wave interactions," *Phys. Fluids* **31**, 081701 (2019).
- <sup>28</sup>D. Lucas, C. P. Caulfield, and R. R. Kerswell, "Layer formation in horizontally forced stratified turbulence: Connecting exact coherent structures to linear instabilities," *J. Fluid Mech.* **832**, 409–437 (2017).
- <sup>29</sup>G. N. Ivey, K. B. Winters, and J. R. Koseff, "Density stratification, turbulence, but how much mixing?," *Annu. Rev. Fluid Mech.* **40**, 169–184 (2008).
- <sup>30</sup>P. Odier and R. E. Ecke, "Stability, intermittency and universal Thorpe length distribution in a laboratory turbulent stratified shear flow," *J. Fluid Mech.* **815**, 243–256 (2017).
- <sup>31</sup>C. J. Lang and M. L. Waite, "Scale-dependent anisotropy in forced stratified turbulence," *Phys. Rev. Fluids* **4**, 044801 (2019).
- <sup>32</sup>T. Hanson, M. Stastna, and A. Coutino, "Stratified shear instability in the cabbeling regime," *Phys. Rev. Fluids* **6**, 084802 (2021).
- <sup>33</sup>A. Lefauve and P. F. Linden, "Experimental properties of continuously forced, shear-driven, stratified turbulence. Part 2. Energetics, anisotropy, parameterisation," *J. Fluid Mech.* **937**, A35 (2022).
- <sup>34</sup>H. Tennekes and J. L. Lumley, *A First Course in Turbulence* (MIT Press, 1972).
- <sup>35</sup>R. Preisendorfer, "Principal component analysis in meteorology and oceanography," *Elsevier* **17**, 425 (1988).
- <sup>36</sup>P. K. Kundu, I. M. Cohen, and D. R. Dowling, *Fluid Mechanics* (Elsevier, 2016).
- <sup>37</sup>S. Waterman and J. M. Lilly, "Geometric decomposition of eddy feedbacks in barotropic systems," *J. Phys. Oceanogr.* **45**, 1009–1024 (2015).
- <sup>38</sup>B. J. Hoskins, I. N. James, and G. H. White, "The shape, propagation and mean-flow interaction of large-scale weather systems," *J. Atmos. Sci.* **40**, 1595–1612 (1983).
- <sup>39</sup>D. P. Marshall, J. R. Maddison, and P. S. Berloff, "A framework for parameterizing eddy potential vorticity fluxes," *J. Phys. Oceanogr.* **42**, 539–557 (2012).
- <sup>40</sup>T. Tamarin, J. R. Maddison, E. Heifetz, and D. P. Marshall, "A geometric interpretation of eddy Reynolds stresses in barotropic ocean jets," *J. Phys. Oceanogr.* **46**, 2285–2307 (2016).
- <sup>41</sup>M. B. Poulsen, M. Jochum, J. R. Maddison, D. P. Marshall, and R. Nuterman, "A geometric interpretation of southern ocean eddy form stress," *J. Phys. Oceanogr.* **49**, 2553–2570 (2019).
- <sup>42</sup>H. van Haren and L. Gostiaux, "A deep-ocean Kelvin-Helmholtz billow train," *Geophys. Res. Lett.* **37**, L03605, <https://doi.org/10.1029/2009GL041890> (2010).
- <sup>43</sup>P. Hazel, "Numerical studies of the stability of inviscid stratified shear flows," *J. Fluid Mech.* **51**, 39–61 (1972).
- <sup>44</sup>J. S. Turner, *Buoyancy Effects in Fluids* (Cambridge University Press, 1979).
- <sup>45</sup>P. G. Drazin and W. H. Reid, *Hydrodynamic Stability* (Cambridge University Press, 2004).
- <sup>46</sup>W. D. Smyth and J. R. Carpenter, *Instability in Geophysical Flows* (Cambridge University Press, 2019).
- <sup>47</sup>C. Caulfield, "Layering, instabilities, and mixing in turbulent stratified flows," *Annu. Rev. Fluid Mech.* **53**, 113–145 (2021).
- <sup>48</sup>D. Koppel, "On the stability of flow of a thermally stratified fluid under the action of gravity," *J. Math. Phys.* **5**, 963–982 (1964).
- <sup>49</sup>S. P. Haigh and G. A. Lawrence, "Symmetric and nonsymmetric Holmboe instabilities in an inviscid flow," *Phys. Fluids* **11**, 1459–1468 (1999).
- <sup>50</sup>A. Lefauve, J. L. Partridge, Q. Zhou, S. B. Dalziel, C. P. Caulfield, and P. F. Linden, "The structure and origin of confined Holmboe waves," *J. Fluid Mech.* **848**, 508–544 (2018).
- <sup>51</sup>W. D. Smyth, G. P. Klaassen, and W. R. Peltier, "Finite amplitude Holmboe waves," *Geophys. Astrophys. Fluid Dyn.* **43**, 181–222 (1988).
- <sup>52</sup>T. R. Osborn, "Estimates of the local rate of vertical diffusion from dissipation measurements," *J. Phys. Oceanogr.* **10**, 83–89 (1980).
- <sup>53</sup>L. H. Shih, J. R. Koseff, G. N. Ivey, and J. H. Ferziger, "Parameterization of turbulent fluxes and scales using homogeneous sheared stably stratified turbulence simulations," *J. Fluid Mech.* **525**, 193–214 (2005).
- <sup>54</sup>G. D. Portwood, S. M. de Bruyn Kops, and C. P. Caulfield, "Asymptotic dynamics of high dynamic range stratified turbulence," *Phys. Rev. Lett.* **122**, 194504 (2019).
- <sup>55</sup>C. J. Subich, K. G. Lamb, and M. Stastna, "Simulation of the Navier-Stokes equations in three dimensions with a spectral collocation method," *Int. J. Numer. Methods Fluids* **73**, 103–129 (2013).
- <sup>56</sup>A. Alexakis, "On Holmboe's instability for smooth shear and density profiles," *Phys. Fluids* **17**, 084103 (2005).
- <sup>57</sup>J. R. Carpenter, G. A. Lawrence, and W. D. Smyth, "Evolution and mixing of asymmetric Holmboe instabilities," *J. Fluid Mech.* **582**, 103–132 (2007).
- <sup>58</sup>A. K. Kaminski, C. P. Caulfield, and J. R. Taylor, "Transient growth in strongly stratified shear layers," *J. Fluid Mech.* **758**, R4 (2014).
- <sup>59</sup>A. Guha and G. A. Lawrence, "A wave interaction approach to studying non-modal homogeneous and stratified shear instabilities," *J. Fluid Mech.* **755**, 336–364 (2014).
- <sup>60</sup>C. D. Winant and F. K. Browand, "Vortex pairing: The mechanism of turbulent mixing-layer growth at moderate Reynolds number," *J. Fluid Mech.* **63**, 237–255 (1974).
- <sup>61</sup>P. C. Patnaik, F. S. Sherman, and G. M. Corcos, "A numerical simulation of Kelvin-Helmholtz waves of finite amplitude," *J. Fluid Mech.* **73**, 215–240 (1976).
- <sup>62</sup>W. Dong, E. W. Tedford, M. Rahmani, and G. A. Lawrence, "Sensitivity of vortex pairing and mixing to initial perturbations in stratified shear flows," *Phys. Rev. Fluids* **4**, 063902 (2019).
- <sup>63</sup>A. Guha and M. Rahmani, "Predicting vortex merging and ensuing turbulence characteristics in shear layers from initial conditions," *J. Fluid Mech.* **878**, R4 (2019).
- <sup>64</sup>A. Lefauve, J. L. Partridge, and P. F. Linden, "Regime transitions and energetics of sustained stratified shear flows," *J. Fluid Mech.* **875**, 657–698 (2019).
- <sup>65</sup>A. Lefauve, J. L. Partridge, and P. F. Linden, "Research data supporting regime transitions and energetics of sustained stratified shear flows," [Dataset] (2019).
- <sup>66</sup>T. M. Dick and J. Marsalek, *Exchange Flow Between Lake Ontario and Hamilton Harbour* (Environment Canada, Canada Center for Inland Waters, 1973).
- <sup>67</sup>G. A. Lawrence, R. Pieters, L. Zaremba, T. Tedford, L. Gu, S. Greco, and P. Hamblin, "Summer exchange between Hamilton Harbour and Lake Ontario," *Deep Sea Res. Part II* **51**, 475–487 (2004).
- <sup>68</sup>M. Arita and G. H. Jirka, "Two-layer model of saline wedge. I: Entrainment and interfacial friction," *J. Hydraul. Eng.* **113**, 1229–1246 (1987).